In situ variability of mass-specific beam attenuation and backscattering of marine particles with respect to particle size, density, and composition

Griet Neukermans,[a,b,c,d,*] Hubert Loisel,[b,c,d] Xavier Mériaux,[b,c,d] Rosa Astoreca,[e] and David McKee[f]

[a] Management Unit of the North Sea Mathematical Models (MUMM), Royal Belgian Institute for Natural Sciences (RBINS), Brussels, Belgium
[b] Université Lille Nord de France, Lille, France
[c] Université du Littoral Côte d'Opale (ULCO), Laboratoire d'Océanologie et Géosciences (LOG), Wimereux, France
[d] Centre National de la Recherche Scientifique (CNRS), UMR 8187, Wimereux, France
[e] Laboratoire d'Ecologie des Systèmes Aquatiques (ESA), Université Libre de Bruxelles, Brussels, Belgium
[f] Department of Physics, University of Strathclyde, Glasgow, Scotland

Abstract

This study analyzes relationships between concentration of suspended particles represented by dry mass, [SPM], or area, [AC], and optical properties including particulate beam attenuation (c_p), side scattering (b_s), and backscattering (b_{bp}), obtained from an intensive sampling program in coastal and offshore waters around Europe and French Guyana. First-order optical properties are driven by particle concentration with best predictions of [SPM] by b_{bp} and b_s, and of [AC] by c_p. Second-order variability is investigated with respect to particle size, apparent density (dry weight-to-wet-volume ratio), and composition. Overall, the mass-specific particulate backscattering coefficient, b_{bp}^m ($=b_{bp}$:[SPM]), is relatively well constrained, with variability of a factor of 3–4. This coefficient is well correlated with particle composition, with inorganic particles having values about three times greater ($b_{bp}^m = 0.012$ m^2 g^{-1}) than organic particles ($b_{bp}^m = 0.005$ m^2 g^{-1}). The mass-specific particulate attenuation coefficient, c_p^m ($= c_p$:[SPM]), on the other hand, varies over one order of magnitude and is strongly driven (77% of the variability explained) by particle apparent density. In this data set particle size does not affect c_p^m and affects b_{bp}^m only weakly in clear (case 1) waters, despite size variations over one order of magnitude. A significant fraction (40–60%) of the variability in b_{bp}^m remains unexplained. Possible causes are the limitation of the measured size distributions to the 2–302-μm range and effects of particle shape and internal structure that affect b_{bp} more than c_p and were not accounted for.

The inherent optical properties (IOPs, *see* Table 1 for notation and abbreviations) of particles suspended in seawater (e.g., phytoplankton, detritus, heterotrophic bacteria, viruses, and mineral particles) are driven to first order by their concentration. Second-order effects are caused by variations in particle size, material composition (i.e., refractive index), shape, and internal structure. Strong relationships are generally found between IOPs and suspended particulate matter concentration, [SPM] (Babin et al. 2003; Boss et al. 2009*a*), or chlorophyll *a* concentration, [Chl *a*], widely used as an index of phytoplankton biomass (Bricaud et al. 1998; Loisel and Morel 1998). Such relationships were derived from in situ measurements, whereas our present understanding of the effect of particle characteristics on IOPs is mainly based on laboratory measurements and theoretical calculations. For instance, studies investigating optical variability of phytoplankton cells with cell size and refractive index (Morel and Bricaud 1986; Ahn et al. 1992; Vaillancourt et al. 2004) or induced by environmental factors (Stramski and Morel 1990; Stramski et al. 2002) were performed in laboratories. Other laboratory studies focused on optical variability of mineral particles (Volten et al. 1998; Stramski et al. 2007). Studies of optical variability with respect to particle size and refractive index (Morel and Bricaud 1981; Morel and Ahn 1991; Stramski and Kiefer 1991) as well as shape and

structure (Kitchen and Zaneveld. 1992; Gordon and Du 2001; Clavano et al. 2007) were based on theoretical calculations. Assessment of IOP variability in optically complex waters with respect to particle concentration and bulk particle characteristics (e.g., size and composition) has started only recently with the availability of appropriate in situ instrumentation (Babin et al. 2003; Peng and Effler 2007; Woźniak et al. 2010). In this paper, we focus on in situ variability of particulate scattering properties.

It is generally observed that particulate attenuation (c_p), scattering (b_p), and backscattering (b_{bp}) coefficients (units: m^{-1}) increase with concentration of suspended particles. The mass-specific attenuation (c_p^m), scattering (b_p^m), and backscattering (b_{bp}^m) coefficients are expected to vary with the nature of the particles (size, refractive index, structure, shape, and composition). These mass-specific optical coefficients represent an optical cross-section per unit mass in units of m^2 g^{-1}. Understanding their variability is of fundamental importance for radiative transfer studies in marine waters, studies coupling optics with ecosystem and biogeochemical models, in situ monitoring of suspended particle dynamics, as well as for ocean color remote sensing. For instance, b_{bp} normalized by [SPM] or [Chl *a*] strongly influences the remote-sensing retrieval accuracy of [SPM] or [Chl *a*], respectively (Brown et al. 2008; Loisel et al. 2010; Nechad et al. 2010). Suspended particles affect the propagation of light in the ocean and light availability to marine organisms. Direct laboratory measurements of

---

* Corresponding author: g.neukermans@mumm.ac.be

Table 1. Notation and abbreviations.

Symbol	Parameter definition, units
[AC]	Total particle projected area concentration, m^{-1}
$[AC]_i$	Particle projected area concentration in the ith bin of the LISST
a_p	Particulate absorption coefficient, m^{-1}
b_p	Particulate scattering coefficient, m^{-1}
b_p^m	b_p:[SPM], mass-specific scattering coefficient, $m^2\ g^{-1}$
b_{bp}	Particulate backscattering coefficient, m^{-1}
$\tilde{b}_{bp}$	Backscattering ratio, b_{bp}:b_p, dimensionless
b_{bp}^m	b_{bp}:[SPM], mass-specific backscattering coefficient, $m^2\ g^{-1}$
b_s	Side scattering coefficient, relative to a formazine particle suspension, FNU
b_s^m	b_s:[SPM], mass-specific side scattering coefficient, FNU $m^3\ g^{-1}$
CDOM	Colored dissolved organic matter
[Chl a]	Chlorophyll a pigment concentration, $\mu g\ L^{-1}$
c_p	Particulate beam attenuation coefficient, m^{-1}
c_p^m	c_p:[SPM], mass-specific beam attenuation coefficient, $m^2\ g^{-1}$
D_A	Mean particle diameter, weighted by area, μm
D_i	Mean diameter of the ith LISST size class, μm
γ	Hyperbolic slope of the particle number concentration size distribution
IQR	Interquartile range, difference between 75th and 25th percentile value
MPE	Median relative prediction error, *see* Web Appendix for definition
$N(D)dD$	Number of particles in the size range D to dD, dimensionless
$N(D_i)$	Number of particles in the ith LISST size class per unit volume and per unit diameter increment, $\mu L\ L^{-1}\ \mu m^{-1}$
N	Real part of the refractive index, relative to water, dimensionless
n_o	Total number of observations
n_x	Number of outliers, identified as described in the Web Appendix
[PIC]	Particulate inorganic carbon concentration, $\mu g\ L^{-1}$
[PIM]	Particulate inorganic matter concentration, $g\ m^{-3}$
[POC]	Particulate organic carbon concentration, $\mu g\ L^{-1}$
[POM]	Particulate organic matter concentration, $g\ m^{-3}$
PPE	Prediction percentile error
PSD	Particle size distribution
Q_{bb}	Backscattering efficiency, dimensionless
Q_{bbe}	Mean backscattering efficiency, weighted by area, dimensionless
Q_{bse}	Mean side scattering efficiency, weighted by area, FNU m^{-1}
Q_c	Attenuation efficiency, dimensionless
Q_{ce}	Mean attenuation efficiency, weighted by area, dimensionless
ρ_a	Particle population mean apparent density (dry weight:wet volume), $kg\ L^{-1}$
ρ_{ag}	Aggregate apparent density (dry weight:aggregate interstitial volume), $kg\ L^{-1}$
ρ_{ap}	Solid particle apparent density (dry weight:particle internal fluid volume), $kg\ L^{-1}$
RMSE	Root mean square error (*see* Web Appendix)
[SPM]	Suspended particulate matter concentration, $g\ m^{-3}$
[VC]	Total volume concentration of particles, $\mu L\ L^{-1}$
$[VC]_i$	Volume concentration of particles in the ith LISST size class, $\mu L\ L^{-1}$

biogeochemical components are not practically feasible at the spatial and temporal scales required to validate ecosystem and biogeochemical models. Optical measurements can be used to accommodate this need.

Since the early 1970s, when the first commercial transmissometers became available, relationships between [SPM] (in $g\ m^{-3}$) and c_p or b_p have been examined in open ocean and coastal waters (Gibbs 1974; Carder et al. 1975; Pak and Zaneveld 1977). Values of c_p^m or b_p^m reported in the literature vary over one order of magnitude, from 0.05 $m^2\ g^{-1}$ to 1.5 $m^2\ g^{-1}$ (Baker and Lavelle 1984; Wells and Kim 1991; Gardner et al. 2001, but *see* Hill et al. 2011 for a comprehensive overview). Theoretical and experimental work focused on the effect of particle size on c_p^m and b_p^m (Pak et al. 1970; Spinrad et al. 1983; Baker and Lavelle 1984). However, despite large variability in particle

size, in situ measurements of c_p^m vary much less (Bunt et al. 1999; Mikkelsen and Pejrup 2000). The recent modeling work of Boss et al. (2009*b*) suggests that the process of particulate aggregation, the formation of flocs composed of mineral and organic particles with water trapped in between, constrains the sensitivity of c_p^m to particle size. This hypothesis is supported by in situ measurements of Hill et al. (2011). Inverse relationships between b_p^m and particle diameter may, however, be found when particles are less aggregated (Woźniak et al. 2010).

An explanation of the observation that b_p^m is significantly lower in coastal waters ($\approx$ 0.5 $m^2\ g^{-1}$) than in open ocean waters ($\approx$ 1 $m^2\ g^{-1}$) was given by Babin et al. (2003) on the basis of Mie scattering calculations, modeling marine particles as homogeneous, solid spheres. In coastal waters, where mineral material is more common than organic

material, the larger apparent density, ρ_{ap} (particle dry weight : wet volume), of the former counterbalances the effect of its higher refractive index. This explanation has, however, been challenged by several studies (Martinez-Vicente et al. 2010; Woźniak et al. 2010). Seasonal changes of b_p^m in a low-turbidity station in the western English Channel have been related to the composition of particulate organic matter, POM (Martinez-Vicente et al. 2010). Bowers et al. (2009) show that the variability of b_p^m in a shallow shelf sea dominated by mineral aggregates is mainly explained by changes in the aggregate apparent density, ρ_{ag} (dry weight : wet volume ratio of material in the aggregate), whereas particle size has only little effect on b_p^m. Note that there is a difference between ρ_{ap} and ρ_{ag}. Whereas wet volume in ρ_{ap} refers to the particle internal fluid volume, it refers to the aggregate interstitial fluid volume in ρ_{ag}. Hill et al. (2011) suggest that the large range of c_p^m and b_p^m values are caused by variability in particle composition, size, and the finite acceptance angle of the optical instruments. Also, [SPM] has been measured using various protocols with varying filter pore sizes, filter types, and corrections for residual salts. The choice of statistical approach (e.g., simple descriptive statistics vs. regression analysis) may also influence the apparent range of variability of normalized IOPs (*see* McKee et al. 2009 for similar effects on the particulate backscattering-to-scattering ratio, $\tilde{b}_{bp}$).

Much less is known about the relationship between b_{bp} and [SPM], the variability of b_{bp}^m, and even about the sources of b_{bp} itself. This is due to a lack of an appropriate theoretical framework for modeling b_{bp} and of commercial in situ sensors for determination of b_{bp} that became available only since the mid-1990s. Our understanding of the major contributors to b_{bp} in natural waters is uncertain and it is unknown which particles backscatter light most efficiently (Stramski et al. 2004). Mie scattering theory suggests substantial contributions to b_{bp} from submicron particles (Stramski and Kiefer 1991), but there is strong evidence that application of this model is inappropriate for computations of b_{bp} for natural particle assemblages (Bohren and Singham 1991; Kitchen and Zaneveld 1992; Clavano et al. 2007). In situ measurements of bulk and size-fractionated measurements of b_{bp} in the open ocean showed strong contributions to b_{bp} from particles larger than 3 μm and negligible contributions from particles below 0.2 μm (Dall'Olmo et al. 2009).

Studies of the relationship between b_{bp} and [SPM] are not always consistent. Some studies show good correlations between b_{bp} and [SPM] (Boss et al. 2009a), whereas others find better correlations with particulate inorganic matter concentration ([PIM]) than with [SPM] (Deyong et al. 2009; Martinez-Vicente et al. 2010). McKee and Cunningham (2006) observed good correlations between b_{bp} and both [SPM] and [PIM] in mineral-dominated turbid waters in the Irish Sea, whereas much weaker correlations were found in clear, more organic-dominated waters. Snyder et al. (2008) show evidence of spatial variability of b_{bp}^m along the U.S. coast and found significant differences between the mass-specific coefficients b_{bp} : [PIM] and b_{bp} : [POM], where [POM] is the particulate organic matter concentration, and [SPM] = [PIM] + [POM]. Several studies in U.S.

coastal waters showed that [SPM] correlates better with b_{bp} than with c_p or b_p (Snyder et al. 2008; Boss et al. 2009a). The projected surface area concentration of suspended particles, [AC], is also known to correlate well with b_{bp}. On the basis of a laboratory experiment, Hatcher et al. (2001) found b_{bp} to increase with [AC] of phytoplankton–mud aggregates larger than 10 μm, despite a drop in [SPM]. Flory et al. (2004) found b_{bp} to linearly increase in situ with [AC] of aggregates larger than 100 μm.

Various types of instruments are available to obtain the particle size distribution (PSD), such as electrical impedance particle sizers (Coulter Counter), laser diffractometers (laser in situ scattering and transmissometry device, Sequoia Scientific, LISST), and particle imaging systems (FlowCAM), but none of these instruments operates over the full optically significant size range from submicron particles to large millimeter-sized flocs. Electron microscopy could cover a broader range (including submicron particles), but is hampered by complex sample preparation, treatment, and analysis (Wells and Goldberg 1994; Peng and Effler 2007, 2010). The LISST-100X instrument series offer several advantages including rapid in situ measurements over relatively large volumes of water and coverage of a broad size range (1.25–250 μm for type B and 2.5–500 μm for type C). Also, unlike the Coulter Counter and the FlowCAM, there is no need for discrete water sampling or sample handling, which may disrupt fragile aggregates. LISST instruments have been shown to provide PSDs that are comparable with other sizing instruments over a wide range of environmental particle types (Agrawal et al. 2008; Andrews et al. 2010; Reynolds et al. 2010). However, to obtain particle size information, an optical model needs to be assumed for inversion of the angular pattern of near-forward scattered light recorded by the LISST. Assumptions on the refractive index of the particles significantly affect the retrieved PSD (Andrews et al. 2010), especially for particles below 20 μm. Other disadvantages of the LISST are its lower size resolution and hence its inability to detect narrow features in the PSD (Reynolds et al. 2010).

Despite recent availability of the required optical instrumentation, studies combining measurements of optical properties of marine particles with investigations of the fundamental causes driving their variability (particle size, apparent density, refractive index, and composition) are rare. Particularly, investigations of optical variability with respect to particle size are limited by the lack of measurements of the PSD over the full optically significant size range. Coverage of submicron particles is of special concern, given that under typical conditions in the open ocean and at 550 nm Mie theory predicts dominant contributions (70–90%) to b_{bp} and significant contributions (up to 50%) to c_p (Stramski and Kiefer 1991). Fractionation experiments in open ocean and coastal waters, however, suggest contributions from submicron particles to b_{bp} of only 10–30% and a much greater importance of particles larger than 3 μm of 53% ± 7% (at 470 nm, Dall'Olmo et al. 2009) and about 70% (at 440 nm, Roesler and Boss 2008), respectively.
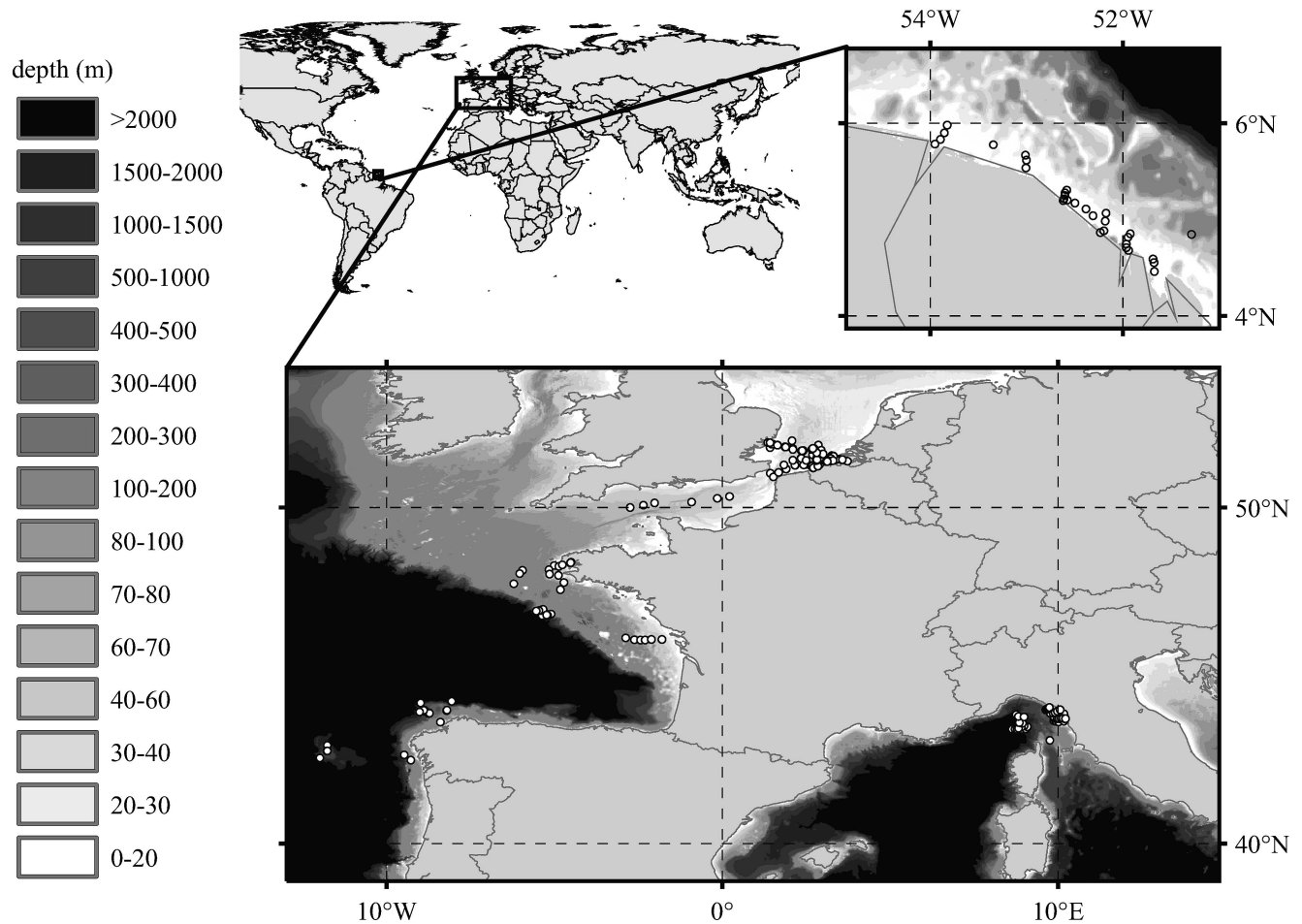
Fig. 1.   Location of stations sampled during 14 campaigns between April 2008 and July 2010. Bathymetry is also shown (source: General Bathymetric Chart of the Oceans, GEBCO_08 30' Grid, version 20100927, http://www.gebco.net).

In the present study, we present and analyze combined measurements of in situ optical properties, particle concentration, apparent density, composition, and size distribution (obtained with a LISST, covering the size range 2.4–302 μm). An intensive sampling program (366 stations) in optically complex coastal and more offshore waters around Europe and French Guyana was carried out. Optical properties (c_p, b_s, and b_{bp}), [SPM], and the PSD were determined by the same people using the same instruments and protocols. The objectives are to reinvestigate the relationships between optical properties (c_p, b_s, and b_{bp}) and proxies of particle concentration, such as [SPM] and [AC]. We also investigate the feasibility of assessing variability of b_{bp}^m and c_p^m with respect to bulk particle composition, apparent density, and size.

Methods

Description of the study areas—Fourteen sampling campaigns in coastal and offshore waters were conducted between April 2008 and July 2010, covering a wide variety of suspended particles in terms of concentration, composition, and size. A total of 366 stations was visited: 213 in the southern North Sea and the English Channel (April,

June, July 2008, 2009, and 2010; September 2008 and 2009; January 2010), 59 in the northeast Atlantic Ocean (June 2008, 2009 and 2010), 60 in the Ligurian Sea (March 2009), and 34 in French Guyana waters (October 2009). A map of the sampling locations is shown in Fig. 1.

The southern North Sea and the English Channel are shallow sea regions, rarely deeper than 50 m, subject to strong semidiurnal tidal currents with a typical amplitude of 1 m s^{-1}. Particles in suspension originate from various sources, including coastal and sea-bottom erosion, river discharges, inflow from the Atlantic Ocean, atmospheric dust, and dredging operations. A decrease of [SPM] with distance from the coast is generally observed, from above 100 g m^{-3} in the nearshore waters to below 0.5 g m^{-3} in the deepest offshore waters. The cruise periods in the southern North Sea cover the bloom onset, development, and collapse of the prymnesiophyte *Phaeocystis globosa* and the dinoflagellate *Noctiluca scintillans*, as well as periods of lower biological activity. Particle composition shows high seasonal variability (Loisel et al. 2007; Astoreca et al. 2009; Martinez-Vicente et al. 2010).

The northeastern Atlantic waters between the Bay of Biscay and the Galicia Bank are typically case 1 waters with IOPs driven by phytoplankton and associated materials.

Water samples were taken on and off the continental shelf with water depths varying between 20 and 300 m and [SPM] usually below 2 g m^{-3}. In June 2010, a bloom of an as yet unidentified heliozoan species occurred (F. Gomez pers. comm.). The Ligurian Sea between Corsica and northwest Italy is typically case 1, though a number of case 2 stations were sampled close to the Italian coast near the Arno River outflow. Samples were taken on and off the continental shelf with water depths varying between 30 and 500 m.

The French Guyana coastal waters are turbid and their IOPs are mainly driven by mineral particles of terrestrial origin (Loisel et al. 2009). These waters are strongly influenced by the Amazon river and affected by local features such as mud banks (Froidefond et al. 2002, 2004; Vantrepotte et al. in press).

Optical measurements—At each station, an optical profiling package was deployed in surface waters for several minutes, followed by a vertical profile from the surface to 2–3 m above the bottom. The package included a conductivity–temperature–depth profiler (Sea Bird), a Western Environmental Technology Laboratory (WET Labs) ECO BB-9 backscattering instrument, a WET Labs ECO-Fl chlorophyll fluorometer, a WET Labs C-Star transmissometer for beam attenuation, a WET Labs ac-s for hyperspectral attenuation and absorption measurements, and a Sequoia Scientific LISST-100X (type C) device for PSD and beam attenuation measurements. The ac-s was equipped with a SeaBird 3K pump with a coarse mesh steel screen for water flow into the 10-cm path-length tubes. Data from the WET Labs instruments were collected and recorded with a WET Labs data handler (DH-4) as a function of time for each of the instruments, enabling simultaneous collection, time stamping, storage, and merging of data from different instruments. The sampling frequency of all instruments was 1 Hz. At each station and for each instrument, about 100–200 surface water scans were collected and median averaged. The difference between the 75th and 25th percentile value, known as the interquartile range (IQR), was taken as a measure of dispersion. These statistics are more robust to outliers than the mean and the standard deviation.

Beam attenuation (c) is calculated from light transmission (T), which is the light intensity reaching a detector through a sample relative to a blank. Let l be the path length of the instrument, then $c = -l^{-1} \ln(T)$. The C-Star measures c at 660 nm ($\pm$ 20 nm) over a 10-cm path length and has an in-water acceptance angle of 1.2°. The C-Star instrument was calibrated by WET Labs on a yearly basis and additional calibrations with MilliQ water were carried out three times per campaign. After calibration, the C-Star measurement directly gives c_p (units: m^{-1}), assuming that colored dissolved organic matter does not absorb at 660 nm. In addition to near-forward scattering (which is inverted to provide particle size information as described in the next section), the LISST records c at 670 nm ($\pm$ 0.1 nm) over a 5-cm path length with an in-water acceptance angle of 0.0135°. The LISST gives c_p after calibration with MilliQ water performed before and after each campaign assuming that CDOM does not absorb at 670 nm.

The ac-s records the absorption and attenuation spectrum at 4-nm resolution between 400 and 730 nm with 15-nm bandwidth, has a 10-cm path length, and an in-water acceptance angle of 0.93°. A MilliQ water calibration was performed before and after each campaign. Temperature and salinity corrections were performed on the raw data (Pegau et al. 1997), and absorption measurements were corrected for residual scattering following Sullivan et al. (2006).

During two selected campaigns, a WET Labs ac-9 instrument was deployed vertically on a bench in the wet lab of the ship. Surface water sampled simultaneously with the optical package was passed through the measuring tubes manually. The instrument measures absorption and attenuation in nine bands: 412, 440, 488, 510, 555, 630, 650, 676, and 715 nm, has a 25-cm path length, and an in-water acceptance angle of 0.93°. A water calibration using MilliQ water was performed on a daily basis. Data were recorded for 2 min, and then median-averaged over 0.5 min of noise-free data. Temperature and salinity were recorded together with the data using a Hanna digital thermometer and a Seabird thermosalinometer SBE-21, respectively. Temperature and salinity corrections, as well as a residual scattering correction, were performed similarly to the ac-s measurements.

Backscattering coefficients $b_b(\lambda)$ at nominal wavelengths of 488, 510, 532, 595, 650, 676, 765, and 865 nm were collected with the ECO BB-9. The instrument records the volume-scattering function, β, at a fixed angle in the backward direction (124°, M. Twardowski pers. comm.). Data conversion from raw β to calibrated β was performed using the WAP software provided by WET Labs. Data were corrected for temperature and absorption effects and the contribution by pure water (Zhang et al. 2009) to β was subtracted to obtain particulate volume-scattering function, β_p. Particulate backscattering coefficients, b_{bp}, were obtained from β_p by multiplying by $2\pi\chi$, with $\chi = 1.1$ (Sullivan and Twardowski 2009). The BB-9 instrument was calibrated by WET Labs on a yearly basis. An additional correction of b_{bp} by a factor 0.82 ($= 0.9 : 1.1$) was applied following Sullivan et al. (2005).

Turbidity, defined by ISO 7027 (1999) as "the reduction of transparency of a liquid caused by the presence of undissolved matter," can be quantified in various ways (e.g., Secchi disk, light attenuation, side scatter). The Hach 2100P portable turbidity instrument measures the ratio of light scattered at an angle of 90° at a wavelength of 860 nm to forward transmitted light, as compared with the same ratio for a standard suspension of formazine. This optical measurement technique of turbidity from the side-scattering coefficient, b_s, is in accordance with ISO 7027 (1999). Turbidity, or b_s, expressed in formazine nephelometric units (FNU), was recorded on 10-mL subsamples in triplicate before and after filtration. These replicates were median averaged and the IQR was computed.

The spectral dependency of c_p or b_{bp} is beyond the scope of this paper and has been investigated by other authors (Snyder et al. 2008). Instead, we focus on c_p and b_{bp} at a wavelength of 650 nm, where the attenuation by particles ($c_p = a_p + b_p$) is essentially determined by their scattering

properties because a_p, the absorption by living and nonliving particles, only makes a very small contribution (Loisel and Morel 1998). For example, in this data set (272 observations) the median contribution of a_p to c_p is 1.5%, with a maximum of 6%.

Water sampling—At each station, water samples were collected just below the sea surface with 10-liter Niskin bottles simultaneously with in situ optical measurements. [SPM] was determined gravimetrically (Van der Linde 1998) by filtration of a known volume of seawater onto 47-mm Whatman GFF glass fiber filters with a nominal pore size of 0.7 μm, which effectively retain particles larger than about 0.4 μm in size. The filters were preashed at 450°C for 1 h, gently washed in 0.5 liters of MilliQ water, dried at 75°C for 1 h, preweighed on a Sartorius LE 2445 analytical balance with an accuracy of 0.1 mg, and stored in a desiccator for use within 2 weeks. Seawater samples were filtered immediately after collection on triplicate filters. To remove salt, filters were washed with 250 mL of MilliQ water after filtration. The samples were stored at −20°C until further analysis in MUMM's Marine Chemistry Laboratory, usually within a few months after sampling. Filters were dried for 24 h at 50°C and reweighed to obtain [SPM]. All SPM filtrations were carried out by G.N. in triplicate using the same protocol. From these, the median and IQR were computed for each sample. Observations where the IQR exceeded 45% of the median [SPM] value were rejected. Concentration of Chl *a* and other pigments was determined by high-performance liquid chromatography analysis. Water samples were filtered in duplicate through 0.7-μm Whatman 47-mm GFF glass fiber filters, which were stored in liquid nitrogen until analysis in the laboratory. Pigment data were then averaged.

During some selected campaigns (92 stations) the SPM sample filters were burned for 5 h at 450°C and then reweighed to obtain [PIM] and [POM] by difference. From April 2010 onward, seawater samples were analyzed for concentration of particulate organic ([POC]) and inorganic ([PIC]) carbon determined with a Thermo scientific carbon/hydrogen/nitrogen (CHN) elemental analyzer. Note that [SPM] includes all organic and mineral material above approximately 0.5–0.7 μm and [POC] and [POM] include autotrophic organisms, heterotrophic bacteria, and detritus. Observations were classified into clear (case 1) and turbid (case 2) waters using the relationship between b_{bp} (532 nm) and [Chl *a*] established by Loisel et al. (2010): b_{bp} = 0.00299 × [Chl *a*]$^{0.704}$. On the basis of their in situ data set, the threshold between case 1 and case 2 waters was set at b_{bp} = 3 × 0.00299 × [Chl *a*]$^{0.704}$.

Particle size and mean apparent density—The scattering pattern at a wavelength of 670 nm in 32 logarithmically spaced scattering angles in the near-forward direction is recorded with a Sequoia Scientific LISST-100X type C described by Agrawal and Pottsmith (2000). The volume concentration for each of its 32 particle size classes is obtained through inversion of the angular forward-scattering pattern based on the principles of light diffraction. This inversion has traditionally been done using

Sequoia Scientific's inversion matrix based on a combination of Mie theory calculations (applicable strictly to homogeneous spherical particles) for several refractive indices.

Recently, empirically based inversion techniques for random-shaped particles became available (Agrawal et al. 2008). The term "random shaped" refers to the particles not having a preferred axis, excluding platy or elongated particles, and can be thought of as "spherical surfaces with random bumps, scratches, and digs superimposed" (Agrawal et al. 2008). This inversion mitigates the problem of an artificial rising tail at the fine-particle end of the number concentration PSD. This artifact was first attributed to particle shape effects by Agrawal et al. (2008), but Andrews et al. (2010) attributed it to a mismatch between the refractive index of small particles and the refractive index of the inversion matrix.

Although all aforementioned LISST inversions assume that particles are solid, the LISST has been found to size aggregates as well, if sufficiently opaque (Hill et al. 2011; Slade et al. 2011). This is consistent with Latimer's (1985) modeling of an aggregate as a combination of a particle with lower index of refraction and a coated particle.

The random-shape inversion matrix (Agrawal et al. 2008) was used in this study, giving volume concentration, [VC]$_i$ (in μL L^{-1}), in each size class *i* with geometric mean diameter D_i in the range 2–350 μm. Note that Mie inversion shifts the size range to 2.5–500 μm for a type C LISST 100X operating at a wavelength of 670 nm. Basic MATLAB scripts for data processing, provided by Sequoia Scientific, were adapted by G. Neukermans for adequate data quality control, custom data processing, and visualization purposes. LISST data have been reported to show considerable instability in the smallest and largest size ranges (Traykovski et al. 1999; Jouon et al. 2008), likely due to the presence of particles smaller and coarser than the measured size range. Hence, data from the outer and inner rings were excluded from further analysis. Instability in the smallest size ranges has also been related to effects of stray light (Reynolds et al. 2010; Andrews et al. 2011).

Assuming spherical particles, the cross-sectional area concentration of particles in size bin *i*, [AC]$_i$ (in m^{-1}), can be obtained from [VC]$_i$:

$$[AC]_i = \frac{3}{2D_i}[VC]_i \qquad (1)$$

where $2 \leq i \leq 31$ and 2.4 μm $\leq D_i \leq$ 302.1 μm. The total cross-sectional area and volume concentrations, [AC] and [VC], are obtained by summation over size classes 2 to 31. Andrews et al. (2010) compared [AC] and [VC] derived from a LISST 100X (type B) using various inversion matrices against microscopy data for phytoplankton and mixed field samples. They report ratios of LISST-derived [AC] and [VC] obtained with the random-shape matrix inversion to microscopy-derived [AC] and [VC] within the ranges of 0.56–0.98 and 0.34–1.08, respectively.

The mean apparent density of the suspended particle population, ρ_a (in kg L^{-1}), is the dry weight-to-wet-volume ratio:

$$\rho_a = \frac{[\text{SPM}]}{[\text{VC}]} \tag{2}$$

The wet volume concentration, [VC], can refer to both the particle internal fluid volume as well as the aggregate interstitial volume. Note that particles with diameter above approximately 0.4 μm are retained on a GFF glass fiber filter (effective pore size of 0.7 μm), whereas [VC] only accounts for particles in the 2.4–302-μm range.

Marine particles are comprised of water and solid material. Let V_s and V_w be the volumes of solid and watery material, respectively, of which a particle is comprised and ρ_s be the density of the solid material. Then, ρ_a can be written as:

$$\rho_a = \frac{V_s}{V_s + V_w} \rho_s \tag{3}$$

When the particle contains any water, ρ_a will be less than ρ_s and can be less than the density of seawater. For phytoplankton ρ_s varies between 1.24 and 1.53 kg L^{-1} and V_w between 40% and 80% (Aas 1996), giving ρ_a between 0.25 and 0.92 kg L^{-1}. For aggregated particles consisting of organic or inorganic compounds (or both), V_w is mostly interstitial and size dependent (Boss et al. 2009*b*) and can approach 100% for the largest aggregates. This results in ρ_a as low as 0.01 kg L^{-1}.

A Junge power law distribution was fitted to the LISST data:

$$N(D_i) = K D_i^{-\gamma} \tag{4}$$

with $2 \le i \le 31$, where $N(D_i)$ is the number of particles in size class i per unit volume and per diameter increment and γ is called the Junge parameter. The size distribution of marine particles is influenced by various physical and biological processes, so it is unlikely that its full complexity can be completely described by a relatively simple mathematical model such as the Junge model. This model, however, remains the most frequently used in optical studies. Its goodness of fit is evaluated by the R^2 statistic, the relative deviation of the model from the observations, and the 95% confidence interval on the least-square estimation of γ. Typical values of γ range between 3 and 5 (Jonasz 1983; Buonassissi and Dierssen 2010; Reynolds et al. 2010).

For a given particle population we define the mean diameter weighted by area, D_A (in μm), as follows:

$$D_A = \frac{\sum\limits_{i=2}^{31} [AC]_i D_i}{[AC]} \tag{5}$$

In sedimentology, this is termed the Sauter diameter.

Mass-specific attenuation and backscattering coefficients—For a population of spherical particles of identical ρ_a, the mass-specific beam attenuation coefficient, c_p^m (or analogously, the mass-specific particulate backscattering coefficient, b_{bp}^m), can be written as:

$$c_p^m = \frac{c_p}{\rho_a[\text{VC}]} = \frac{\frac{\pi}{4}\int N(D)Q_c(D, n, \lambda)D^2 dD}{\rho_a \frac{\pi}{6}\int N(D)D^3 dD} \tag{6}$$

where $N(D)dD$ is the number of particles per unit volume in the size range from D to $D + dD$ and Q_c (dimensionless) is the attenuation efficiency factor, which varies with size (D), wavelength (λ), and refractive index (n) of the particles (Van de Hulst 1957). This efficiency factor is dimensionless and represents the ratio of the attenuation (backscattering) cross-section to the geometric cross-section.

The refractive index, n, can be estimated from the particulate backscattering ratio $\tilde{b}_{bp}$ using the Mie theory-based model of Twardowski et al. (2001):

$$n = 1 + 1.671\tilde{b}_{bp}^{0.582} \tag{7}$$

This model performs reasonably well for $\gamma < 4$, with differences of only a few percent between Eq. 7 and the more complex model for n based on $\tilde{b}_{bp}$ and γ (Twardowski et al. 2001). Equation 7 is preferred here for the sake of simplicity and presentation purposes and because γ exceeds 4 in only 5% of the cases in our data set. The particulate backscattering ratio, $\tilde{b}_{bp}$, represents the fraction of light scattered in the backward direction and has been related to the biogeochemical composition ([POC]:[Chl *a*]) of the particles (Loisel et al. 2007) and to the PSD (Ulloa et al. 1994; Loisel et al. 2007).

Consider a particle population composed of spheres of a single diameter D; then Eq. 6 simplifies to:

$$c_p^m = \frac{3}{2}\frac{Q_c}{\rho_a D} \tag{8}$$

For particle populations consisting of spheres of identical composition and density it follows that c_p^m is inversely proportional to particle diameter. For particles large compared with the wavelength of light, smaller particles attenuate more light per unit mass than large particles because their surface-to-volume ratio is larger (e.g., Hill et al. 2011). We can rewrite Eq. 6 in the form of Eq. 8 by defining the effective attenuation efficiency, Q_{ce}, the mean attenuation efficiency of all particles weighted by area (Eq. 3.2 in Morel 1973; Bowers et al. 2009):

$$Q_{ce} = \frac{\int N(D)Q_c(D)D^2 dD}{\int N(D)D^2 dD} \tag{9}$$

and $D_A = \frac{\int N(D)D^3 dD}{\int N(D)D^2 dD}$, the mean particle diameter weighted by area, which is equivalent to Eq. 5. Eq. 6 then becomes:

$$c_p^m = \frac{3}{2}\frac{Q_{ce}}{\rho_a D_A} \tag{10}$$

The coefficient c_p^m (in m^2 g^{-1}) is also the attenuation cross-section per unit mass of particles in suspension. Equation 6 and Eqs. 8–10 can be written for backscattering in the same way. Q_{ce} can be assessed either directly from its definition,

i.e., $Q_{ce} = c_p$: [AC] (*see* Eq. 6), or indirectly, from linear regression between c_p^m and the inverse of the product of ρ_a and D_A (*see* Eq. 10). Computations of Q_{bbe} can be done by analogy.

The experimental value of Q_{ce} (= c_p : [AC]) can be used to check whether the bulk of the particles contributing to c_p are sized by the LISST, through a comparison with its theoretical value (Behrenfeld and Boss 2006). According to optical theory, the value of Q_c for a single spherical particle large compared with the wavelength of the light should be around 2 and not exceed 3.2 (Van de Hulst 1957). Underestimation of [AC] will lead to higher Q_{ce} values. The first cause of underestimation of [AC] is the limited size range of the PSD (2.4–302 μm in this study). Oubelkheir et al. (2005) reported c_p : [AC] ratios up to 14 due to particles outside their PSD range (1.6–50 μm). The second cause is the underestimation of [AC] of particles that are sized by the LISST. Andrews et al. (2010) report underestimates of LISST-derived [AC] values obtained from an inversion for random-shape particles compared with microscopy-derived [AC] values by a factor of 1.02 to 1.79. Therefore, a maximum value for c_p : [AC] of 5.7 (= 3.2 $\times$ 1.79) is expected if the bulk of the particles are sized by the LISST. Observations exceeding this maximum value are rejected.

From Eq. 10 it follows that particle size, density, and composition affect c_p^m (b_{bp}^m) directly through D_A and ρ_a, and indirectly through Q_{ce} (Q_{bbe}). The effect of size, density, and composition on mass- and area-specific c_p and b_{bp} is investigated in this paper. Correlation analysis and "least squares cubic" regressions (York 1966), which take into account measurement uncertainties in the data, are used throughout the paper. The derivation of uncertainties on optical and biogeochemical variables is given in the Web Appendix at www.aslo.org/lo/toc/vol_57/issue_1/0124a.pdf. The least-squares cubic regression is applied after removal of outliers identified by the MATLAB robustfit.m routine (*see* Web Appendix for details). Correlation coefficients obtained from bootstrapping are given with their 95% confidence intervals, which is also described in the Web Appendix.

Results

Intercomparison of c_p *obtained with different instruments*—c_p, measured by the LISST, C-Star, ac-9, and ac-s instruments, are compared. The first three instruments measure c_p at slightly different wavelengths (670, 660, and 650 nm, respectively). On the basis of 158 spectra of c_p recorded by the ac-s, a median $c_p(650) : c_p(670)$ ratio of 1.01 was found, with 90% of the ratios in the interval [0.99, 1.03], indicating that the spectral variation of c_p between 650 and 670 nm is negligible. Good linearity in log-log space ($r = 0.87 \pm 0.04$) was found for 188 simultaneous observations of c_p(LISST) and c_p(C-Star). Results are shown in Fig. 2A. As expected, c_p(LISST) values are larger than c_p(C-Star) values in most cases because of the smaller acceptance angle of the LISST. Occasionally, however, the C-Star reported higher c_p values than the LISST, possibly due to slight differences in sampling time between the two instruments, high temporal variability of IOPs, and other

measurement uncertainties. The median measurement uncertainty on c_p(LISST) was used as a tolerance distance from the 1:1 line (represented by the dotted line in Fig. 2A), below which observations were removed from further analysis ($n_o = 16$, with n_o denoting the number of observations). The correlation coefficient for the remaining 172 observations is 0.91 ± 0.03. The median c_p(LISST) : c_p(C-Star) ratio is 1.6 with 90% of the ratios in the interval [0.9, 3.3], and increases with increasing particle size as shown in Fig. 2B ($r = 0.88 \pm 0.08$, $n_o = 158$ after removal of observations with $Q_{ce} > 5.7$). Similar results were found by Boss et al. (2009c), who reported a mean LISST-B (acceptance angle of 0.0269°)-to-C-Star c_p ratio of 1.4 (90% in the interval [1.1, 1.8]) at a coastal station in the Northeast of the U.S.A.

Both c_p(ac-s) and c_p(ac-9) are in good agreement with c_p(C-Star), with correlation coefficients of 0.97 ± 0.01 ($n_o = 149$) and 0.98 ± 0.02 ($n_o = 57$), respectively (*see* Fig. 2C). Because of the smaller acceptance angles of the ac-9 and ac-s instruments, data generally lie above the 1:1 line. Some observations, however, are found below the 1:1 line. Recall that the ac-9 measurements were carried out in the wet lab of the ship on seawater sampled simultaneously with the optical profiling package. Small differences in sampling time or depth between the sample bottle and the profiling package may result in ac-9 observations below the 1:1 line. All ac-s observations below the 1:1 line were recorded in April 2010 during a bloom of *P. globosa* colonies. It is hypothesized that these did not entirely pass through the ac-s steel mesh screen on the intakes to the sample chambers of the ac-s, or the pump got clogged by mucilage present in high concentrations during blooms. This analysis suggests that pumping seawater through the chambers of the ac-s can reduce c_p if particles larger than the steel mesh screen size are present or the pump is clogged by mucilage. Boss et al. (2009b) showed that in a coastal environment dominated by aggregates, pumped c_p(LISST-B) was about 30% higher than undisturbed c_p(LISST-B), possibly caused by disruption of aggregates.

c_p, b_s, *and* b_{bp} *vs.* [AC] *and* [SPM]—Relationships and correlations between various IOPs and area ([AC]) and mass ([SPM]) concentration are investigated. Observations are retained where all optical properties (c_p, b_s, and b_{bp}), [SPM], and [AC] were recorded ($n_o = 119$) and where the bulk of the particles were sized by the LISST ($Q_{ce} < 5.7$). A total of 107 data points remain, of which 35 are classified as case 1 and 72 as case 2 waters. The ac-s c_p measurements are not included because of uncertainties on the effect of the steel mesh screen as described above.

Scatter plots of c_p, b_s, and b_{bp} as a function of [SPM] and [AC] in log-log space are shown in Fig. 3. Each parameter covers about two orders of magnitude. All scattering properties correlate well with both area and mass concentration, with correlation coefficients above 0.93 (*see* Table 2). For c_p, no significant differences between correlations with [AC] ($r_{\text{LISST}} = 0.98 \pm 0.01$, $r_{\text{C-Star}} = 0.95 \pm 0.04$) or with [SPM] ($r_{\text{LISST}} = 0.94 \pm 0.04$, $r_{\text{C-Star}} = 0.95 \pm 0.02$) were found. The coefficients b_s and b_{bp} are significantly better correlated with [SPM] ($r_{bs} = 0.988 \pm$
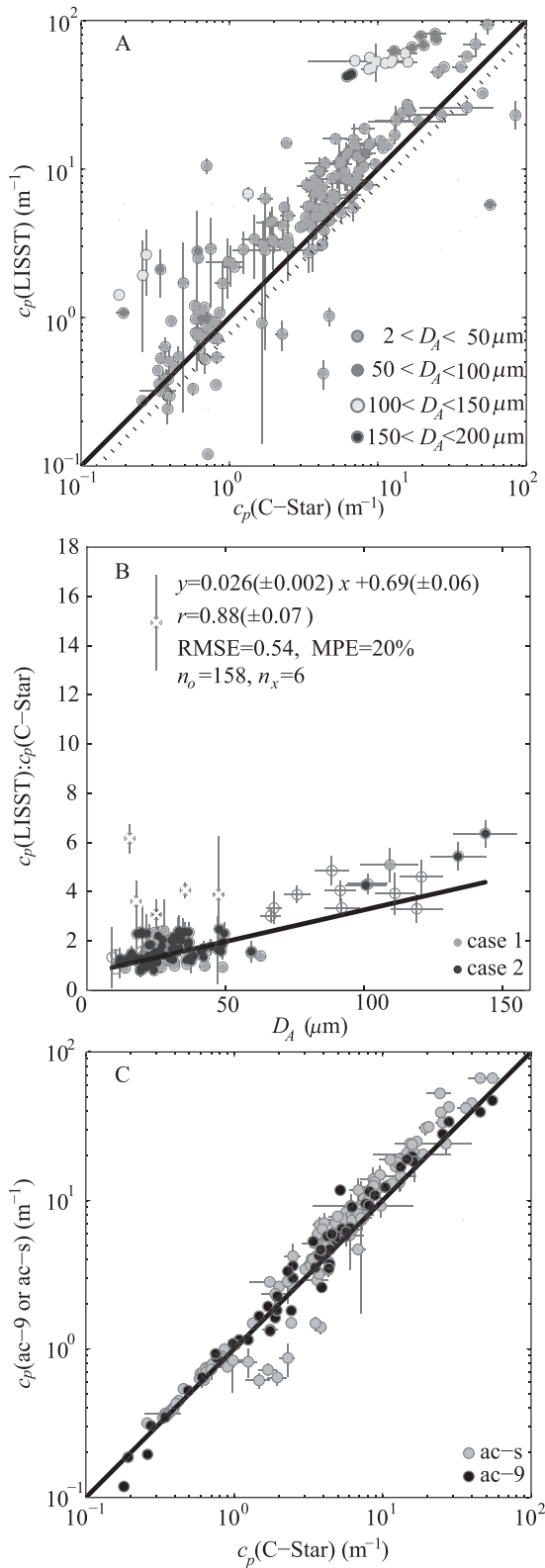
0.007, $r_{bbp} = 0.986 \pm 0.007$) than with [AC] ($r_{bs} = 0.93 \pm 0.05$, $r_{bbp} = 0.92 \pm 0.05$). In the case of b_s, this could be attributed to the fact that the exact same volume of seawater on which b_s was recorded was passed through the filter for determination of [SPM]. Recall that whereas [AC] includes particles between 2.4 and 302 μm, [SPM] is the mass concentration of particles larger than approximately 0.4 μm. The lower correlation of b_{bp} with [AC] than with [SPM] might be attributed to differences in particle size ranges covered by each parameter. These include particles smaller than 2.4 μm, which are thought to be important contributors to b_{bp} assuming particles are homogeneous spheres (Stramski et al. 2004), and particles larger than 302 μm, which may contribute substantially to b_{bp} (Hatcher et al. 2001; Flory et al. 2004).

Flory et al. (2004) studied the relationship between b_{bp} and [AC] for flocs larger than 100 μm during the onset, development, and collapse of a spring phytoplankton bloom in Nova Scotia. Their b_{bp} and [AC] data ranges were comparable with this study. They report $b_{bp}(589\ nm)$:[AC] values as the slope of a b_{bp} vs. [AC] regression with a value of 0.012 ± 0.001 before the bloom when particles were mainly inorganic, and 0.0029 ± 0.0001 during and after the bloom when the suspended particulate matter was dominated by larger organic particles and aggregates. In this study we find higher values of 0.041 ± 0.003 for case 2 waters (with median n of 1.15, 90% in the interval [1.10, 1.20], $n_o = 72$) and 0.012 ± 0.002 for case 1 waters (with median n of 1.07, 90% in the interval [1.04, 1.13], $n_o = 35$).

The 5th, 50th, and 95th percentile values of the ratios of optical properties to area and mass concentration are shown in Table 2. Rejecting the 10% most extreme values, $Q_{ce}(LISST)$, that is, $c_p(LISST)$:[AC], varies by about a factor of 2 between 1.86 and 4.54, whereas $c_p^m(LISST)$ covers almost one order of magnitude ranging between 0.36 and 3.46. Comparable results are observed for $c_p(C\text{-}Star)$. For b_{bp} and b_s, however, Q_{bbe} (Q_{bse}) spans more than one order of magnitude, whereas b_{bp}^m and b_s^m vary by factors of 3 to 4.

Carder et al. (1975) argued that in the case of solid spherical particles b_p^m would vary less than b_p:[AC] because of the more or less concomitant variations in n and ρ_a. Whereas b_{bp}^m varies less than b_{bp}:[AC], the opposite is observed for c_p^m (which is comparable with b_p^m at 650 nm) and c_p:[AC]. In what follows, the sensitivity of mass-specific (back) scattering to each of the components in Eq. 10 (i.e., particle size, density, efficiency, and composition) is examined. Next, a similar sensitivity analysis is done for efficiency factors of attenuation (Q_{ce}) and backscattering (Q_{bbe}).

Fig. 2. (A) Scatter plot of particulate beam attenuation (c_p) measured simultaneously with LISST and C-Star instruments, coded according to particle size (D_A). The 1:1 line (solid) and the rejection threshold line ($\log_{10}[c_p\{LISST\}]) = \log_{10}(c_p[C\text{-}Star] - 0.1124$, dotted) are shown. (B) Scatter plot of $c_p(LISST)$:$c_p(C\text{-}Star)$ vs. D_A. The type II regression line (*see* Web Appendix for $\leftarrow$ details) is shown, with its equation and statistics. Error bars corresponding to uncertainties above 100% are not shown for clarity. (C) Scatter plot of c_p measured simultaneously by the C-Star and the ac-s or ac-9. The 1:1 line is also shown. On each panel, error bars denote uncertainty estimates as derived in the Web Appendix.
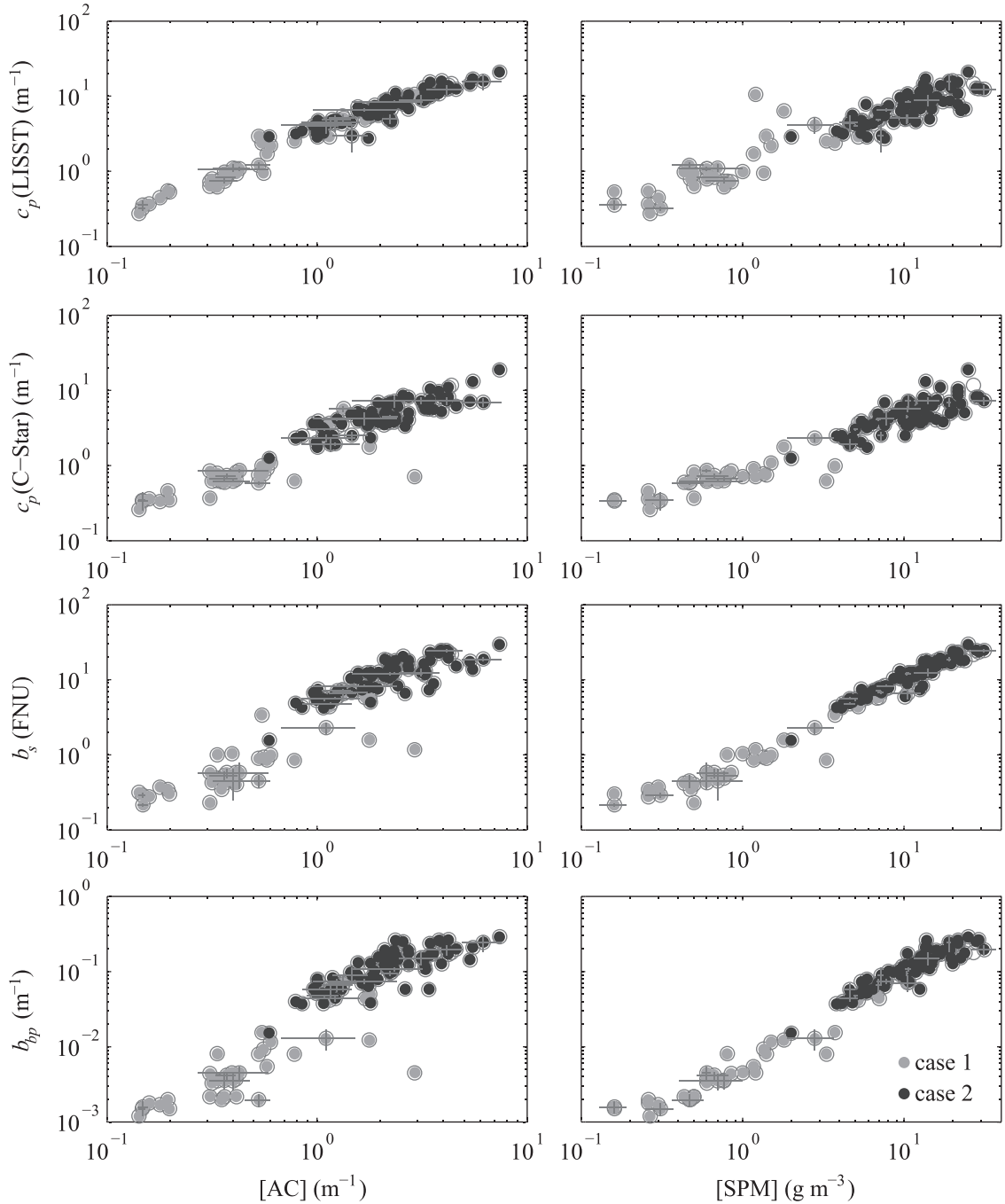
Fig. 3. Log-log scatter plots of c_p(LISST), c_p(C-Star), b_s, and b_{bp} vs. area concentration, [AC] (left column) and mass concentration, [SPM] (right column) for 35 case 1 and 72 case 2 waters. Error bars denote uncertainty estimates as derived in the Web Appendix, shown only for 20 random observations for the sake of clarity.

Mass-specific scattering properties vs. D_A, ρ_a, *efficiency, and composition*—Correlation coefficients, regression equations, and goodness-of-fit statistics for c_p^m(LISST) and b_{bp}^m vs. D_A, ρ_a, efficiency factors, and composition are shown in Table 3. A selection of corresponding scatter plots and best-fit lines are shown in Fig. 4A–G. A large portion of the variability in c_p^m(LISST) is explained by $(\rho_a D_A)^{-1}$ ($r = 0.95 \pm 0.03$, Fig. 4A). Attenuation efficiency factors, Q_{ce}, were obtained from a linear regression of c_p^m and $(\rho_a D_A)^{-1}$

by multiplication of the slope of the regression line in Table 3 by $2:3$ (*see* Eq. 10). Median Q_{ce}(LISST) values of 2.13 ± 0.07 ($r = 0.96 \pm 0.04$) and 3.07 ± 0.02 ($r = 0.84 \pm 0.06$) are obtained for case 1 and case 2 waters, respectively. Bowers et al. (2009) find $Q_{ce} = 1.27 \pm 0.05$ for mainly mineral particles along the south and west coasts of Britain where $b_p^m(670 \text{ nm})$ varied between 0.06 and 1.01 $\text{m}^2\text{ g}^{-1}$. Differences in Q_{ce} could be due to acceptance angle effects.

Table 2. Correlation coefficients (*r* with 95% confidence interval, *see* Web Appendix for details) between an optical property and either area concentration, [AC], or mass concentration, [SPM] (in log-log space), for 107 observations (35 case 1 and 72 case 2). The median, 5th, and 95th percentile values of mass- and area-specific optical properties are shown. Correlations and mass-specific coefficients for all simultaneous observations of an optical property and [SPM] are also shown between brackets (database size, n_t, is indicated in italic).

Parameter	Case (n_t)	r	Population percentile values		
			5	50	95
c_p^m(LISST)	1 (*44*)	0.85±0.10 (0.75±0.16)	0.57 (0.46)	1.40 (1.29)	3.46 (3.73)
	2 (*96*)	0.78±0.08 (0.68±0.12)	0.36 (0.28)	0.71 (0.72)	1.14 (2.99)
	1+2 (*180*)	0.94±0.04 (0.88±0.04)	0.38 (0.31)	0.79 (0.80)	2.22 (3.19)
Q_{ce}(LISST)	1	0.98±0.02	1.86	2.5	4.2
	2	0.92±0.05	2.24	3.35	4.54
	1+2	0.98±0.01	2.03	3.08	4.47
c_p^m(C-Star)	1 (*65*)	0.89±0.09 (0.86±0.08)	0.33 (0.44)	0.97 (0.81)	2.01 (1.79)
	2 (*105*)	0.78±0.08 (0.92±0.03)	0.25 (0.25)	0.45 (0.45)	0.71 (0.78)
	1+2 (*206*)	0.95±0.02 (0.94±0.02)	0.26 (0.25)	0.54 (0.53)	1.39 (1.36)
Q_{ce}(C-Star)	1	0.85±0.18	0.84	1.84	3.04
	2	0.83±0.06	1.31	2.14	3.32
	1+2	0.95±0.04	1.18	2	3.3
b_s^m	1 (*80*)	0.95±0.05 (0.89±0.06)	0.50 (0.57)	0.84 (0.96)	1.34 (1.82)
	2 (*145*)	0.95±0.04 (0.990±0.004)	0.75 (0.79)	1.04 (1.08)	1.30 (1.50)
	1+2 (*333*)	0.988±0.007 (0.987±0.003)	0.63 (0.66)	0.99 (1.08)	1.32 (1.82)
Q_{bse}	1	0.86±0.11	0.77	1.55	4.62
	2	0.83±0.07	2.52	5.3	7.81
	1+2	0.93±0.05	0.98	4.47	7.54
b_{bp}^m	1 (*80*)	0.96±0.03 (0.86±0.06)	0.0038 (0.0038)	0.0054 (0.0069)	0.0097 (0.0127)
	2 (*137*)	0.92±0.04 (0.97±0.01)	0.0067 (0.0065)	0.0100 (0.0104)	0.0141 (0.0152)
	1+2 (*229*)	0.986±0.007 (0.97±0.01)	0.0043 (0.0043)	0.0091 (0.0094)	0.0133 (0.0149)
Q_{bbe}	1	0.83±0.16	0.0041	0.0103	0.034
	2	0.81±0.12	0.0256	0.0489	0.0828
	1+2	0.92±0.05	0.0067	0.0424	0.0797

When the effects of ρ_a^{-1} and D_A^{-1} are considered separately, we find that changes in ρ_a almost entirely control changes in c_p^m(LISST) ($r = 0.88 \pm 0.06$), with denser particles having lower c_p^m, whereas changes in particle size have little influence (*see* Table 3 and Fig. 4B). Bowers et al. (2009) also find that most of the variability in b_p^m is explained by ρ_a (59%) with little contribution from D_A (15%). In case 2 waters, c_p^m(C-Star) increased with decreasing D_A ($r = 0.54 \pm 0.15$ with D_A^{-1}, $n_o = 72$, $p < 0.001$, not shown). This size effect could be caused by the large acceptance angle of the C-Star instrument: the fraction of c_p that is actually detected decreases rapidly with D_A (Boss et al. 2009c), whereas a large fraction of the particle mass might be contained in larger particles to which the C-Star is relatively insensitive.

The relative size independency of c_p^m has been explained by the process of particle aggregation (Boss et al. 2009b; Hill et al. 2011). When particles aggregate and grow in size, they incorporate water in their structure and their density decreases. When ρ_a is inversely proportional to diameter ($\rho_a \propto D_A^{-1}$), it follows from Eq. 10 that c_p^m is independent of size, as pointed out previously by several authors (Hill et al. 1994; Ganju et al. 2006; Curran et al. 2007). The relationship between ρ_a and D_A is shown in Fig. 5. Overall, ρ_a and D_A are inversely related ($r = -0.78 \pm 0.12$, $\rho_a \propto D_A^{-1.24(\pm 0.05)}$, $n_o = 140$). The relationship is tighter in case 2 waters ($r = -0.83 \pm 0.12$,

$\rho_a \propto D_A^{-1.31(\pm 0.05)}$, $n_o = 81$) than in case 1 waters ($r = 0.49 \pm 0.29$, $\rho_a \propto D_A^{-1.30(\pm 0.32)}$, $n_o = 35$).

Significant deviations from the Junge PSD model given in Eq. 4 were observed (not shown). The Junge PSD model generally overestimated number concentrations by up to a factor of 3 at the fine (< 4 μm)- and large (> 60 μm)-particle end of the PSD and underestimated in between. Even though the Junge model provided a relatively poor fit to the measured PSDs, the Junge parameter, γ, can be used as a rough indicator of the relative proportion between the number of small and large particles. No significant correlations are found between c_p^m or b_{bp}^m and γ (*see* Fig. 4C). According to Mie theory, c_p^m should increase over one order of magnitude with increasing γ, and the increase is steeper with increasing real part of the refractive index (*see* gray lines in Fig. 4C from Boss et al. 2009b for a wavelength of 660 nm). If, however, particles are modeled as aggregates rather than solid spheres, c_p^m is rather insensitive to γ (*see* black lines in Fig. 4C from Boss et al. 2009b). Also shown in Fig. 4C are the 10% highest density observations ($n_o = 16$, $\rho_a > 0.45$ kg L^{-1}), which are thought to be least aggregated. These observations show a sharp increase in c_p^m, with γ increasing from 3 to 4 and then a plateau between 4 and 4.5. This is in accordance with Mie theory, although there is an offset in absolute values of c_p^m, possibly due to differences in densities between the model and the in situ measurements. A mean γ of 3.4 ± 0.3 and

Table 3. Correlations and regression analysis of mass-specific attenuation (c_p^m) and backscattering (b_{bp}^m) vs. mean particle diameter (D_A), mean apparent density (ρ_a), mean optical efficiency factors (Q_{ce}, Q_{bbe}), and particle composition. ns, not significant (i.e., $p > 0.05$). *, $p < 0.05$; **, $p < 0.001$, n_o is the number of observations, n_x is the number of outliers removed as described in the Web Appendix.

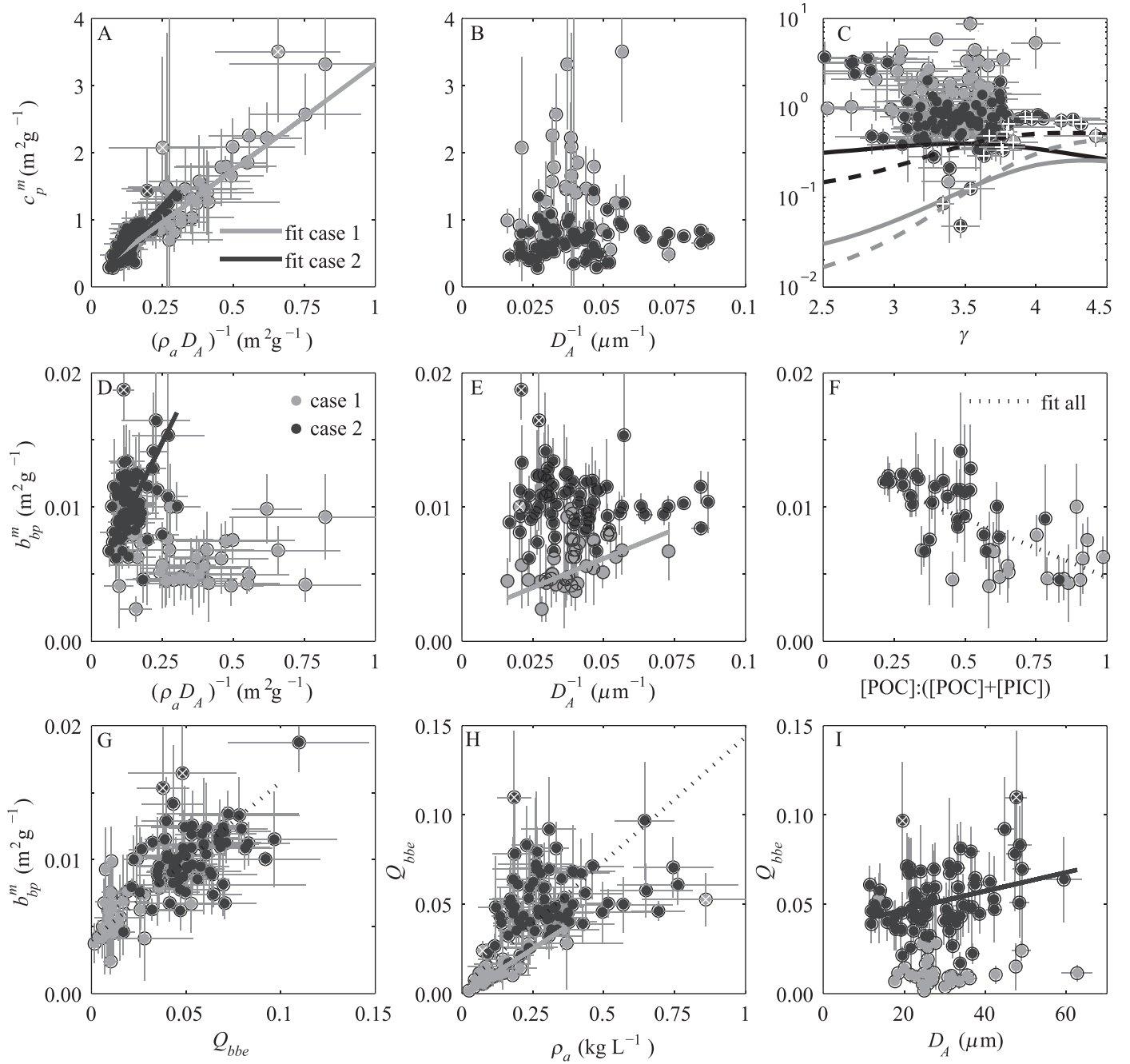| x	case	n_o	c_p^m					b_{bp}^m				
			n_x	r	Equation	RMSE	MPE (%)	n_x	r	Equation	RMSE	MPE (%)
$(\rho_a D_A)^{-1}$	1	35	3	0.96±0.04*	3.2(±0.1)x+0.17(±0.04)	0.23	12	0	ns	—	—	—
	2	72	1	0.84±0.06*	4.6(±0.3)x+0.04(±0.05)	0.13	15	1	0.28±0.23	—	—	—
	1+2	107	4	0.95±0.03*	3.5(±0.1)x+0.18(±0.03)	0.16	13	2	−0.43±0.14*	−0.014(±0.001)x+0.0117(±0.0004)	0.0030	18
ρ_a^{-1}	1	35	5	0.92±0.07*	0.113(±0.007)x+0.29(±0.05)	0.30	12	0	ns	—	—	—
	2	72	1	0.53±0.19*	0.12(±0.01)x+0.21(±0.06)	0.22	22	2	0.36±0.23	—	—	—
	1+2	107	5	0.88±0.06*	0.123(±0.006)x+0.21(±0.04)	0.25	19	2	−0.46±0.12*	−0.0005(±0.0001)x+0.0118(±0.0004)	0.0029	19
D_A^{-1}	1	35	1	ns	—	—	—	1	0.37±0.21*	0.09(±0.03)x+0.002(±0.001)	0.0017	20
	2	72	0	ns	—	—	—	2	ns	—	—	—
	1+2	107	11	ns	—	—	—	1	ns	—	—	—
Q_{ce} or Q_{bbe}	1	35	2	ns	—	—	—	0	0.35±0.28	—	—	—
	2	72	3	0.37±0.22	—	—	—	4	0.43±0.21*	0.11(±0.01)x+0.004(±0.001)	0.0019	11
	1+2	107	11	ns	—	—	—	2	0.76±0.10**	0.12(±0.01)x+0.0040(±0.0004)	0.0020	12
[POC]	1	17	1	ns	—	—	—	0	ns	—	—	—
$\overline{[POC]+[PIC]}$	2	30	1	ns	—	—	—	0	−0.56±0.21*	−0.008(±0.002)x+0.014(±0.001)	0.0018	11
	1+2	47	1	0.51±0.26*	0.95(±0.25)x+0.35(±0.15)	0.35	31	0	−0.64±0.14*	−0.009(±0.002)x+0.014(±0.001)	0.0023	19
$\overline{[POM]}$	1	5	0	ns	—	—	—	0	−0.59±0.38	—	—	—
$\overline{[SPM]}$	2	17	1	ns	—	—	—	0	ns	—	—	—
	1+2	22	2	0.58±0.39	—	—	—	1	−0.43±0.30	—	—	—

Fig. 4.   Scatter plots of mass-specific beam attenuation, c_p^m(LISST) vs. (A) the scattering cross-section (inverse of the product of apparent density and diameter, $[\rho_a D_A]^{-1}$), (B) the inverse of particle diameter weighted by area, D_A^{-1}, and (C) hyperbolic slope of the PSD. Modeling results of Boss et al. (2009*b*) are shown for solid spherical particles (black lines) and for aggregates (gray lines) with refractive indices of $1.05 + 0.0001i$ (solid) and $1.15 + 0.0001i$ (dashed). Scatter plots of mass-specific backscatter, b_{bp}^m vs. (D) $(\rho_a D_A)^{-1}$, (E) D_A^{-1}, (F) [POC] : ([POC] + [PIC]), and (G) backscattering efficiency, Q_{bbe} ($= b_{bp} : [AC]$). Scatter plots of Q_{bbe} vs. ρ_a (H) and D_A (I). Error bars on all panels denote uncertainties as derived in the Web Appendix. Equations and statistics of the fitted lines can be found in Tables 3 and 4.

3.5 ± 0.4 is observed in case 1 and case 2 waters, respectively, which is in close agreement with the mean value of 3.5 found by Reynolds et al. (2010) from many PSDs measured in coastal waters.

Whereas 90% of the variability in c_p^m could be attributed to $(\rho_a D_A)^{-1}$, variability in b_{bp}^m was more difficult to discern

and correlation coefficients for the parameters tested are lower (*see* Table 3). In contrast to c_p^m, variability in b_{bp}^m is not explained well by $(\rho_a D_A)^{-1}$, though there is a clear separation between case 1 and case 2 waters as shown in Fig. 4D. Higher correlations are found between b_{bp}^m and particle composition, as quantified by the ratio of [POC] to
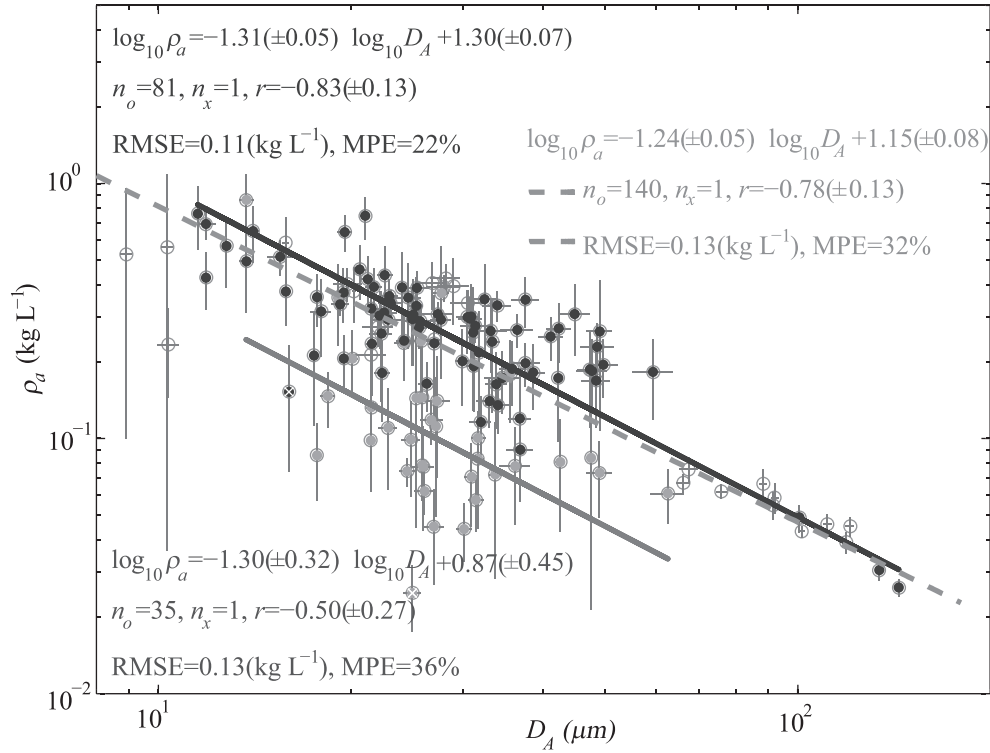
Fig. 5.   Mean particle apparent density (ρ_a) vs. mean particle diameter weighted by area (D_A). The relationship is shown for all data (black circles), for case 1 (gray dots) and case 2 waters (black dots). Statistics and equations of the type II regression lines (*see* Web Appendix for details) fitted to each data set are also shown. Error bars denote uncertainty estimates as derived in the Web Appendix.

the sum of [POC] and [PIC] ($r = -0.64 \pm 0.14$, Table 3). The robust regression line fitted to the pooled data set (case 1 and case 2 waters) is shown in Fig. 4F with equation (*see* also Table 3):

$$b_{bp}^m = -0.009(\pm 0.002) \frac{[POC]}{[POC]+[PIC]} + 0.014(\pm 0.001) \quad (11)$$

Waters dominated by inorganic particles backscatter up to 2.4 times more per unit dry mass ($b_{bp}^m = 0.0121 \pm 0.0023$ m^2 g^{-1}) than waters dominated by organic particles ($b_{bp}^m = 0.0051 \pm 0.0023$ m^2 g^{-1}). The [POC] data set comprises 47 observations in southern North Sea and northeastern Atlantic waters, with D_A ranging between 14 and 49 μm and ρ_a ranging between 0.07 and 0.86 kg L^{-1}. A similar, but weaker, relationship ($r = -0.43 \pm 0.30$) is found for 22 [POM]:[SPM] observations in the southern North Sea, giving the following robust fit:

$$b_{bp}^m = -0.009(\pm 0.003) \frac{[POM]}{[SPM]} + 0.010(\pm 0.001) \quad (12)$$

Here, D_A varied between 23 and 135 μm, ρ_a between 0.04 and 0.39 kg L^{-1}, and [POM]:[SPM] between 20% and 90%. [POM]- and [PIM]-specific b_{bp} vary between 0.001 and 0.05 m^2 g^{-1}, which is in good agreement with the 0.001–0.025 m^2 g^{-1} range reported by Snyder et al. (2008) where [POM]:[SPM] varied between 34% and 70%. Martinez-Vicente et al. (2010) report a b_{bp}(532 nm):[PIM]

of 0.0055 $\pm$ 0.0012 m^2 g^{-1} ($n_o = 16$), at the lower limit of our observations.

In case 1 waters, none of the variables correlated significantly with b_{bp}^m at the $p < 0.001$ level, except particle size (*see* Table 3). Smaller particles with D_A around 15 μm have b_{bp}^m values of 0.0080 $\pm$ 0.0017 m^2 g^{-1} and backscatter about twice as much per unit mass than larger particles with D_A around 50 μm. However, this relationship is weak (*see* Fig. 4E), explaining only 14% of the variability. In case 2 waters no correlation with size is found, which is in accordance with the clay particle aggregation experiment by Slade et al. (2011). Possible causes for lower correlations in case 1 waters are higher contributions to b_{bp} from submicron particles that are not included in the PSD and higher measurement uncertainties compared with case 2 waters.

Whereas no sensitivity of c_p^m to Q_{ce} is found (*see* Table 3), significant positive correlations are found between b_{bp}^m and Q_{bbe} for case 2 waters and pooled case 1 + case 2 waters, with correlation coefficients of 0.43 $\pm$ 0.21 and 0.76 $\pm$ 0.10 respectively. The relationship between b_{bp}^m and Q_{bbe} is shown in Fig. 4G. In what follows we investigate the effect of D_A, ρ_a, and composition on the optical efficiency factors, Q_{ce} and Q_{bbe}.

Attenuation and backscattering efficiency vs. D_A, ρ_a, *and composition*—Correlation coefficients, regression equations, and goodness-of-fit statistics between the optical

efficiency factors (Q_{ce} and Q_{bbe}) and potential drivers of optical variability (D_A, ρ_a, and composition) are shown in Table 4. Both Q_{ce} and Q_{bbe} are mostly driven by particle composition, with correlation coefficients of -0.65 ± 0.14 and -0.69 ± 0.12, respectively. Inorganic-dominated waters with 80% [PIC] have mean Q_{ce} values of 3.6 ± 0.42, which is about twice as high as the mean Q_{ce} value of 2.29 ± 0.42 for organic-dominated waters with 5% [PIC]. Variability of Q_{bbe} covers about one order of magnitude, from 0.007 for organic-dominated waters to 0.067 ± 0.018 for inorganic-dominated waters. No further drivers of Q_{ce} were identified. This efficiency factor did not correlate with particle size and only 15% of its variability could be attributed to ρ_a.

Besides particle composition, other drivers of Q_{bbe} were identified depending on the water type. In case 1 waters, 90% of the Q_{bbe} values range between 0.004 and 0.034 with a median value of 0.010 (*see* Table 2). Vaillancourt et al. (2004) report Q_{bbe} factors at $\lambda = 620$ nm between 0.001 and 0.068, with a mean of 0.011, for 28 phytoplankton cultures with diameters from 1.4 to 35 μm. This is in good agreement with our case 1 observations. About 85% of the variability is attributed to ρ_a (*see* Table 4 and Fig. 4H). The densest particle suspensions ($\rho_a = 0.37$ kg L^{-1}) have mean Q_{bbe} values of 0.036, and backscatter light 20 times more efficiently than porous particle suspensions ($\rho_a = 0.02$ kg L^{-1}). In case 2 waters we find higher Q_{bbe} factors, with 90% of the values ranging between 0.026 and 0.083 and a median value of 0.049. These values correspond well with the Q_{bbe} range of 0.046 to 0.062 and mean value of 0.051 at $\lambda = 650$ nm as reported by Peng and Effler (2010) for mineral particle populations. A small fraction (21%) of the variability in Q_{bbe} is attributed to particle size (*see* Table 4). Since only particles between 2.4 and 302 μm were sized and included in [AC], these results should be interpreted cautiously.

c_p, b_s, *and* b_{bp} *as proxies for* [SPM]—When all observations are considered ($n_o = 366$), regardless of whether information on size or composition is available, optical and [SPM] data each span over three orders of magnitude. The data range is slightly lower for b_{bp} because of saturation of the instrument at high levels of [SPM]. Correlation coefficients and 5th, 50th, and 95th percentile values of mass-specific scattering properties are shown in Table 2. Correlations are similar to the values found for the more limited data set presented in Table 2: b_s correlates best with [SPM], followed by b_{bp} and c_p.

The median c_p^m(C-Star) values are close to the mean b_p^m(555 nm) values of 1 and 0.5 m^2 g^{-1} reported by Babin et al. (2003) for case 1 and case 2 waters, respectively, whereas the c_p^m(LISST) values are about 60% higher because of acceptance angle effects. The best-fit value of McKee and Cunningham (2006) of c_p^m(650 nm, ac-9) = 0.34 ± 0.01 m^2 g^{-1} for mineral-rich case 2 waters in the Irish Sea is at the lower end of our C-Star observations. Values of b_{bp}^m by Martinez-Vicente et al. (2010) and Loisel et al. (2009) at $\lambda = 532$ nm are 0.0034 ± 0.0008 m^2 g^{-1} ($n_o = 19$) and 0.0065 ± 0.0025 m^2 g^{-1} ($n_o = 13$) respectively, and are at the lower end of our observations.

Table 4. Correlations and regression analysis of optical efficiency factors (Q_{ce}, Q_{bbe}) vs. mean particle diameter (D_A), mean apparent density (ρ_a), and particle composition. ns, not significant (i.e., $p > 0.05$). *, $p < 0.001$, n_o is the number of observations, n_x is the number of outliers removed as described in the Web Appendix.

| | | | | Q_{ce} | | | | | Q_{bbe} | | | |
x	case	n_o	n_x	r	Equation	RMSE	MPE (%)	n_x	r	Equation	RMSE	MPE (%)
ρ_a	1	35	1	0.44±0.35	—	—	—	2	0.92±0.11*	0.10(±0.01)x−0.0007(±0.0007)	0.0037	19
	2	72	0	ns	—	—	—	1	0.32±0.19	—	—	—
	1+2	107	1	0.39±0.13*	4.4(±0.5)x+2.0(±0.1)	0.82	16	6	0.63±0.11*	0.14(±0.01)x+0.004(±0.004)	0.0203	42
D_A	1	35	1	ns	—	—	—		ns	—	—	—
	2	72	0	ns	—	—	—	2	0.46±0.18*	0.0001(±0.0002)x+0.04(±0.01)	0.0182	21
	1+2	107	0	ns	—	—	—	0	ns	—	—	—
[POC]	1	17	0	−0.63±0.23*	−2.5(±0.8)x+4.5(±0.6)	0.59	18	4	ns	—	—	—
	2	30	1	ns	—	—	—	0	−0.59±0.19*	−0.08(±0.02)x+0.09(±0.01)	0.016	21
[POC]+[PIC]	1+2	47	2	−0.65±0.14*	−1.7(±0.3)x+3.9(±0.2)	0.42	10	0	−0.69±0.12*	−0.08(±0.01)x+0.083(±0.007)	0.018	29
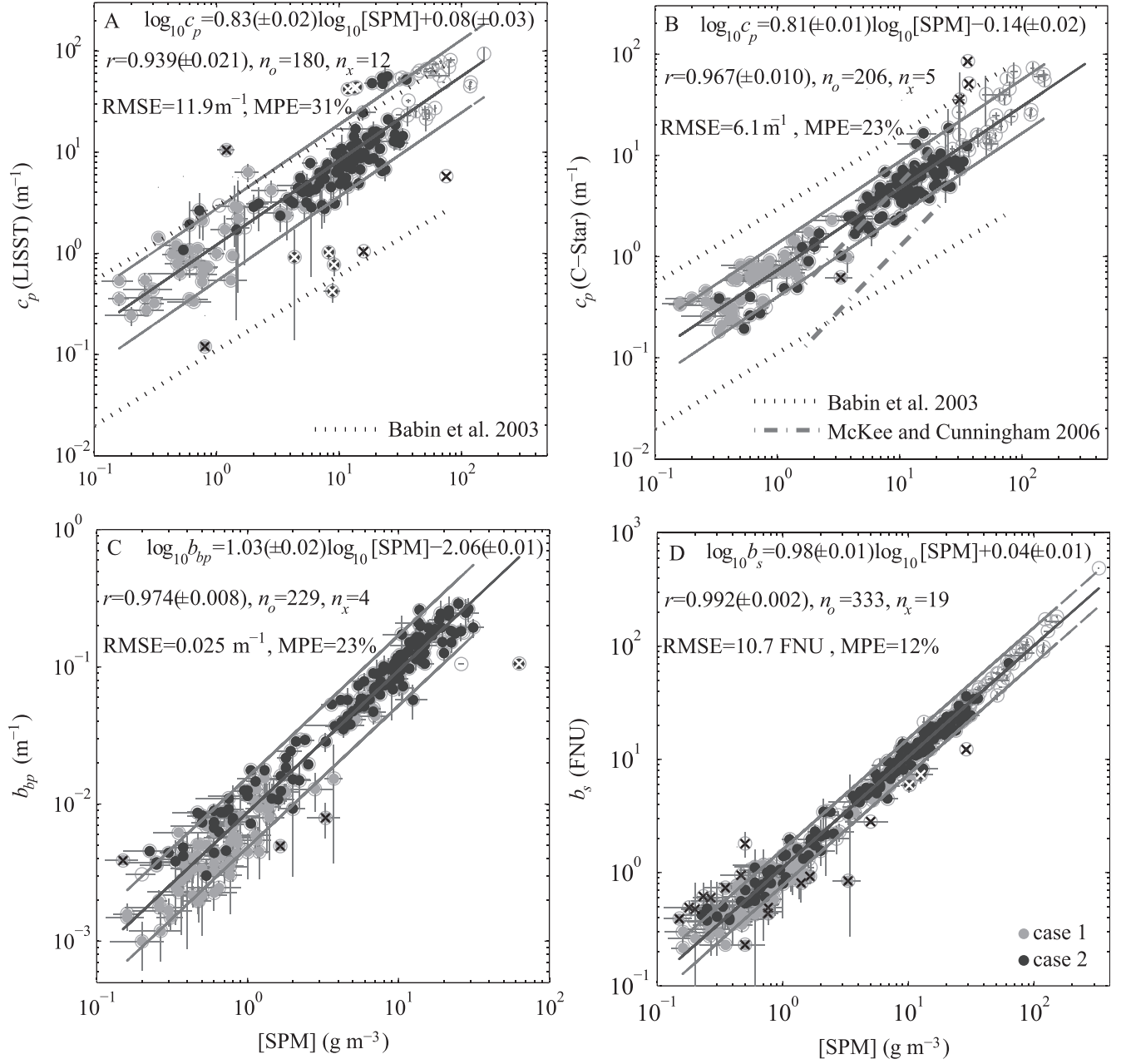
Fig. 6. Scatter plots of (A) c_p(LISST), (B) c_p(C-Star), (C) b_{bp}, and (D) b_s vs. [SPM]. Robust regression lines are shown in black, together with their 90% prediction bounds, equations and statistics. (A, B) For comparison, the 90% prediction bounds of the c_p(676 nm)-[SPM] data of Babin et al. (2003) and the c_p(650 nm)-[SPM] data of McKee and Cunningham (2006).

Scatter plots of c_p(LISST), c_p(C-Star), b_{bp}, and b_s as a function of [SPM] for all available data are shown in Fig. 6. On each plot, the least-squares regression line, its 90% prediction bounds, equation, and statistics are also shown. For comparison, the 90% prediction bounds of the c_p(676 nm, ac-9) vs. [SPM] data from Babin et al. (2003) are also indicated in Fig. 6A,B, as well as the c_p(650 nm, ac-9) vs. [SPM] data from McKee and Cunningham (2006). The effect of the smaller acceptance angle of the ac-9 instrument used by Babin et al. (2003) is clearly visible in Fig. 6A.

To compare the performance of c_p, b_s, and b_{bp} as proxies for [SPM], data points where all optical properties and [SPM] were recorded were retained ($n_o = 126$). Linear regression prediction models for [SPM] were established. All scattering properties are relatively good predictors of [SPM], with correlation coefficients above 0.90. Model performances were evaluated through comparison of the ratio of the absolute difference between [SPM] from regression and its observed value to its observed value, the prediction percentile error (PPE). Results are shown in Table 5. In 50% and 95% of the cases, a b_{bp}-based [SPM]

Table 5. Optical properties as proxies for [SPM]. Prediction percentile error, PPE, i.e., the ratio of the absolute value of the difference between a type II regression model-derived [SPM] and its observed value to its observed value. Values between brackets for an optical model with $1.2 < $ [SPM] $ < 82.4$ g m^{-3} for our data set and for the data set of Boss et al. (2009*a*) in italic. *r* is the correlation coefficient with its 95% confidence interval (*see* Web Appendix for details).

PPE	*r*	Population percentiles (%)		
		5	50	95
c_p (LISST)	0.90 ± 0.05	4	37	283
c_p (C-Star)	0.95 ± 0.01 (0.89±0.04, *0.970±0.005*)	4 (3, *2*)	32 (29, *16*)	107 (59, *54*)
b_s	0.990 ± 0.006 (0.97±0.02, *0.962±0.008*)	1 (1, *2*)	11 (10, *21*)	41 (37, *51*)
b_{bp}	0.987 ± 0.006 (0.96±0.02, *0.982±0.005*)	1 (1, *1*)	18 (17, *9*)	47 (44, *36*)

model agrees with the observed [SPM] within 18% and 47%, respectively. The b_s-based [SPM] model performs best, predicting [SPM] within 41% of its true value in 95% of the cases. Boss et al. (2009*a*) found b_{bp} to be the best proxy for [SPM], followed by b_s and c_p. Their comparison was based on 85 samples from the eastern and western coasts of North America with [SPM] ranging between 1.2 and 82.4 g m^{-3}. For comparison with Boss et al. (2009*a*), PPEs obtained from our observations covering the same [SPM] range are shown between brackets in Table 5 ($n_o = 98$), as well as the PPEs and correlation coefficients found by those authors. In the present study, b_s was recorded on a subsample of the Niskin seawater sample, which might explain the better performance of the b_s-based model compared with models based on optical properties recorded in-water.

Discussion

In this study, we show that first-order variability of c_p, b_{bp}, and b_s is driven by particle concentration with best predictions of dry mass concentration, [SPM], by b_{bp} and b_s and of surface area concentration, [AC], by c_p. Second-order variability of c_p and b_{bp} was investigated with respect to the nature of the particles in suspension through analysis of variability in mass-specific (c_p^m and b_{bp}^m) and area-specific coefficients in response to changes in particle composition, size, and density. PSDs were derived from a LISST particle sizer, covering the size range 2.4–302 μm. We have shown that the variability of c_p^m(LISST) covers more than one order of magnitude from 0.28 to 3.45 m^2 g^{-1}. About 90% of its variability is due to the direct combined effect of particle apparent density and size, $(\rho_a \times D_A)^{-1}$, with the strongest contribution coming from ρ_a, which explains 77% of the variability. The coefficient b_{bp}^m shows less variability with 90% of the observations varying by a factor of 3–4 between 0.004 and 0.014 m^2 g^{-1}. Factors driving variability in b_{bp}^m are more difficult to discern, although particle composition, which acts indirectly on b_{bp}^m via Q_{bbe}, explains about 40% of the variability. Inorganic particles are, on average, about two to three times more efficient per unit mass ($b_{bp}^m = 0.012$ m^2 g^{-1}) than organic particles ($b_{bp}^m = 0.005$ m^2 g^{-1}).

Carder et al. (1975) reasoned that for solid spherical particles b_p^m would vary less than b_p:[AC] because of the more or less concomitant variations in *n* and ρ_a. Figure 7 shows the variability of $\tilde{b}_{bp}$ (related to *n* via Eq. 7) with ρ_a

and particle composition. Significant correlations are found between $\tilde{b}_{bp}$ (and *n*) and particle composition, as quantified by (1) [POC]:([POC] + [PIC]), with $r = -0.62 \pm 0.15$ and $n_o = 48$ (*see* Fig. 7A), (2) [POM]:[SPM], with $r = -0.65 \pm 0.19$ and $n_o = 23$ (*see* Fig. 7B), and (3) [POC]:[SPM], with $r = -0.75 \pm 0.09$ in log-log scale and $n_o = 48$ (*see* Fig. 7D). These relationships agree with expectations of low *n* (1.02–1.10) for particles dominated by organic material (Aas 1996) and higher *n* (1.15–1.22) for inorganic particles (Woźniak and Stramski 2004). Both $\tilde{b}_{bp}$ and *n* are positively correlated with ρ_a with correlation coefficients (in log-log scale) of 0.75 ± 0.09 for 111 observations (*see* Fig. 7C).

Since *n* increases with ρ_a, optical efficiency factors (Q_{bbe}, Q_{ce}) and ρ_a will compensate each other in Eq. 10 if they are sufficiently sensitive to *n* (particle composition) and if the mass-normalized optical property shows sufficient sensitivity to optical efficiency. The coefficient c_p^m shows no sensitivity to Q_{ce}, hence variability in c_p^m is almost entirely controlled by $\rho_a \times D_A$. This explains the order-of-magnitude variability in c_p^m observed in this study. In the case of b_{bp}^m, Q_{bbe} and ρ_a compensate each other (*see* Fig. 4H and Tables 3, 4), which explains why b_{bp}^m shows less variability.

Potential drivers of mass-specific optical properties were identified via Eq. 10. These are particle composition (via optical efficiency), ρ_a, and D_A. Although 90% of the variability in c_p^m is explained by variations in the denominator, $\rho_a \times D_A$, this approach was not so successful in explaining variability in b_{bp}^m. Only 40–60% of the variability in b_{bp}^m could be explained, and even less in case 1 waters. Possible causes are uncertainties in the assessment of $Q_{bbe} \times (\rho_a \times D_A)^{-1}$ due to the limited size range covered by the LISST PSD, and the potential inappropriateness of Eq. 10 for b_{bp}^m due to sensitivity to particle shape and internal structure.

We recall that ρ_a and D_A are derived from a PSD between 2.4 and 302 μm (Eqs. 2 and 5). Mie theory predicts that the contribution of submicron particles, which are not included in the PSD, to b_{bp} is significant and higher than for c_p (Stramski and Kiefer 1991). Experimental results, on the other hand, show that their significance for b_{bp} may be overstated (Roesler and Boss 2008; Dall'Olmo et al. 2009) and that the homogeneous spherical model is inappropriate for modeling b_{bp} (Kitchen and Zaneveld 1992; Clavano et al. 2007).

We further note that Eq. 10 is based on sphericity of the particles, material homogeneity across the PSD, and the assumption that IOPs can be related to bulk particle
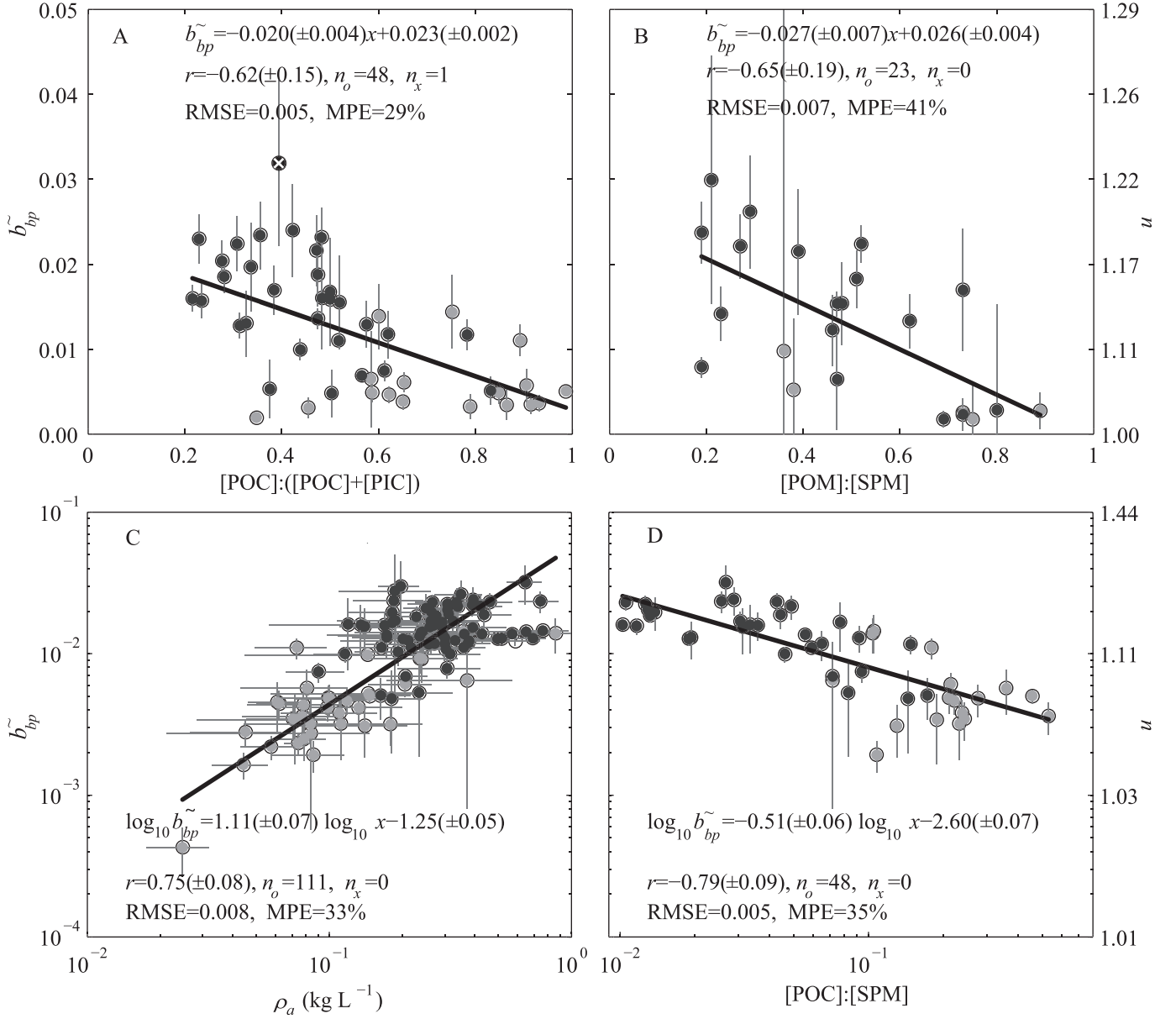
Fig. 7. Scatter plots of the backscattering ratio, $\tilde{b}_{bp}$ ($= b_{bp} : c_p[\text{LISST}]$) vs. (A) [POC] : ([POC] + [PIC]), (B) [POM] : [SPM], (C) mean apparent density (ρ_a), and (D) [POC] : [SPM]. Regression lines, with equations and statistics, are shown on each panel (*see* Web Appendix for details). Case 1 waters are shown in gray and case 2 waters in black. Error bars denote uncertainty estimates as derived in the Web Appendix.

properties. It is known that nonsphericity and a heterogeneous interior of particles affect light scattered in the backward direction more than when integrated over all directions (Kitchen and Zaneveld 1992; Clavano et al. 2007). Hence, Eq. 10 may be inappropriate in the case of b_{bp}.

PSDs obtained with a LISST are affected by the assumed optical model, particularly by the assumed index of refraction of the particles. A priori knowledge of particle composition, however, does not necessarily improve the accuracy of LISST-derived PSDs (Andrews et al. 2010). Overall, Mie-based models with low indices of refraction, such as Sequoia's Mie composite model, lead to artificially

high concentrations of small particles, whereas models assuming a high index of refraction, such as Sequoia's random-shape inversion model used here, do not have this artifact (Agrawal et al. 2008; Andrews et al. 2010). A Mie model with inorganic refractive index was found to produce the most accurate results for PSD shape, [AC], and [VC] (Andrews et al. 2010). Theoretical models allowing for more realistic particle shapes and structures than homogeneous spheres are expected to help improve the accuracy of LISST PSDs, but concerns remain about small out-of-range particles (Andrews et al. 2010) and effects of stray light, particularly for surface-water deployments (Reynolds et al. 2010; Andrews et al. 2011).

Efforts to explain the in situ variability of b_{bp}^m may be more successful with acquisition of PSDs over the full range of optically significant particles, from submicron-sized particles to large aggregates several millimeters in diameter, and inclusion of particle shape and internal structure information. Underwater digital holographic particle imaging sensors, such as Sequoia's LISST-HOLO operating over the 25–2500-μm size range, have become available recently and research is ongoing for extension of these systems into the submicron range (A. Nimmo-Smith and M. Twardowski pers. comm.). These sensors may offer new capabilities for obtaining PSDs, including information on complex particle shapes and structures that will facilitate development of new models relating IOPs to PSDs.

References

AAS, E. 1996. Refractive index of phytoplankton derived from its metabolite composition. J. Plankton Res. **18:** 2223–2249, doi:10.1093/plankt/18.12.2223

AGRAWAL, Y. C., AND H. C. POTTSMITH. 2000. Instruments for particle size and settling velocity observations in sediment transport. Mar. Geol. **168:** 89–114, doi:10.1016/S0025-3227(00)00044-X

———, A. WHITMIRE, O. A. MIKKELSEN, AND H. C. POTTSMITH. 2008. Light scattering by random-shaped particles and consequences on measuring suspended sediments by laser diffraction. J. Geophys. Res. **113:** C04023, doi:10.1029/2007JC004403

AHN, Y. H., A. BRICAUD, AND A. MOREL. 1992. Light backscattering efficiency and related properties of some phytoplankters. Deep-Sea Res. I **39:** 1835–1855, doi:10.1016/0198-0149(92)90002-B

ANDREWS, S., D. NOVER, AND S. G. SCHLADOW. 2010. Using laser diffraction data to obtain accurate particle size distributions: The role of particle composition. Limnol. Oceanogr.: Methods **8:** 507–526, doi:10.4319/lom.2010.8.507

ANDREWS, S. W., D. M. NOVER, K. E. REARDON, J. E. REUTER, AND S. G. SCHLADOW. 2011. The influence of ambient light intensity on in situ laser diffractometers. Water Resour. Res. **47:** W06509, doi:10.1029/2010WR009841

ASTORECA, R., V. ROUSSEAU, K. RUDDICK, C. KNECHCIAK, B. VAN MOL, J. Y. PARENT, AND C. LANCELOT. 2009. Development and application of an algorithm for detecting *Phaeocystis globosa* blooms in the case 2 southern North Sea waters. J. Plankton Res. **31:** 287–300, doi:10.1093/plankt/fbn116

BABIN, M., A. MOREL, V. FOURNIER-SICRE, F. FELL, AND D. STRAMSKI. 2003. Light scattering properties of marine particles in coastal and open ocean waters as related to the particle mass concentration. Limnol. Oceanogr. **48:** 843–859, doi:10.4319/lo.2003.48.2.0843

BAKER, E. T., AND J. W. LAVELLE. 1984. The effect of particle size on the light attenuation coefficient of natural suspensions. J. Geophys. Res. **89:** 8197–8203, doi:10.1029/JC089iC05p08197

BEHRENFELD, M. J., AND E. BOSS. 2006. Beam attenuation and chlorophyll concentration as alternative optical indices of phytoplankton biomass. J. Mar. Res. **64:** 431–451, doi:10.1357/002224006778189563

BOHREN, C. F., AND S. B. SINGHAM. 1991. Backscattering by nonspherical particles—a review of methods and suggested new approaches. J. Geophys. Res. **96:** 5269–5277, doi:10.1029/90JD01138

BOSS, E., AND OTHERS. 2009a. Comparison of inherent optical properties as a surrogate for particulate matter concentration in coastal waters. Limnol. Oceanogr.: Methods **7:** 803–810, doi:10.4319/lom.2009.7.803

———, W. SLADE, AND P. HILL. 2009b. Effect of particulate aggregation in aquatic environments on the beam attenuation and its utility as a proxy for particulate mass. Opt. Express **17:** 9408–9420, doi:10.1364/OE.17.009408

———, W. H. SLADE, M. BEHRENFELD, AND G. DALL'OLMO. 2009c. Acceptance angle effects on the beam attenuation in the ocean. Opt. Express **17:** 1535–1550, doi:10.1364/OE.17.001535

BOWERS, D. G., K. M. BRAITHWAITE, W. A. M. NIMMO-SMITH, AND G. W. GRAHAM. 2009. Light scattering by particles suspended in the sea: The role of particle size and density. Cont. Shelf Res. **29:** 1748–1755, doi:10.1016/j.csr.2009.06.004

BRICAUD, A., A. MOREL, M. BABIN, K. ALLALI, AND H. CLAUSTRE. 1998. Variations of light absorption by suspended particles with chlorophyll a concentration in oceanic (case 1) waters: Analysis and implications for bio-optical models. J. Geophys. Res. **103:** 31033–31044, doi:10.1029/98JC02712

BROWN, C. A., Y. HUOT, P. J. WERDELL, B. GENTILI, AND H. CLAUSTRE. 2008. The origin and global distribution of second-order variability in satellite ocean color and its potential applications to algorithm development. Remote Sens. Environ. **112:** 4186–4203, doi:10.1016/j.rse.2008.06.008

BUNT, J. A. C., P. LARCOMBE, AND C. F. JAGO. 1999. Quantifying the response of optical backscatter devices and Transmissometers to variations in suspended particulate matter. Cont. Shelf Res. **19:** 1199–1220, doi:10.1016/S0278-4343(99)00018-7

BUONASSISSI, C. J., AND H. M. DIERSSEN. 2010. A regional comparison of particle size distributions and the power law approximation in oceanic and estuarine surface waters. J. Geophys. Res. **115:** C10028, doi:10.1029/2010JC006256

CARDER, K. L., J. BEARDSLEY, F. GEORGE, AND H. PAK. 1975. Physical, chemical and optical measures of suspended-particle concentrations: Their intercomparison and application to the West African Shelf, p. 173–193. *In* R. J. Gibbs [ed.], Suspended solids in waters. Plenum.

CLAVANO, W. R., E. BOSS, AND L. KARP-BOSS. 2007. Inherent optical properties of non-spherical marine-like particles—from theory to observation. Oceanogr. Mar. Biol. **45:** 1–38, doi:10.1201/9781420050943.ch1

CURRAN, K. J., P. S. HILL, T. G. MILLIGAN, O. A. MIKKELSEN, B. A. LAW, X. DURRIEU DE MADRON, AND F. BOURRIN. 2007. Settling velocity, effective density, and mass composition of

suspended sediment in a coastal bottom boundary layer, Gulf of Lions, France. Cont. Shelf Res. **27:** 1408–1421, doi:10.1016/j.csr.2007.01.014

DALL'OLMO, G., T. K. WESTBERRY, M. J. BEHRENFELD, E. BOSS, AND W. H. SLADE. 2009. Significant contribution of large particles to optical backscattering in the open ocean. Biogeosciences **6:** 947–967, doi:10.5194/bg-6-947-2009

DEYONG, S., L. YUNMEI, W. QIAO, J. GAO, L. HENG, L. CHENGFENG, AND H. CHANGCHUN. 2009. Light scattering properties and their relation to the biogeochemical composition of turbid productive waters: A case study of Lake Taihu. Appl. Opt. **48:** 1979–1989, doi:10.1364/AO.48.001979

FLORY, E. N., P. S. HILL, T. G. MILLIGAN, AND J. GRANT. 2004. The relationship between floc area and backscatter during a spring phytoplankton bloom. Deep-Sea Res. I **51:** 213–223, doi:10.1016/j.dsr.2003.09.012

FROIDEFOND, J. M., L. GARDEL, D. GUIRAL, M. PARRA, AND J. F. TERNON. 2002. Spectral remote sensing reflectances of coastal waters in French Guiana under the Amazon influence. Remote Sens. Environ. **80:** 225–232, doi:10.1016/S0034-4257(01)00301-7

———, F. LAHET, C. HU, D. DOXARAN, D. GUIRAL, M. T. PROST, AND J. F. TERNON. 2004. Mudflats and mud suspension observed from satellite data in French Guiana. Mar. Geol. **208:** 153–168, doi:10.1016/j.margeo.2004.04.025

GANJU, N. K., D. H. SCHOELLHAMER, M. C. MURRELL, J. W. GARTNER, AND S. A. WRIGHT. 2006. Constancy of the relation between floc size and density in San Francisco Bay, p. 75–91. *In* J. P. Maa, L. H. Sanford, and D. H. Schoellhamer [eds.], Estuarine and coastal fine sediment dynamics—INTERCOH 2003. Elsevier.

GARDNER, W. D., AND OTHERS. 2001. Optics, particles, stratification, and storms on the New England continental shelf. J. Geophys. Res. **106:** 9473–9497, doi:10.1029/2000JC900161

GIBBS, R. J. 1974. Sediment transport model for Amazon river Atlantic Ocean. Trans. Am. Geophys. Union **55:** 279–279.

GORDON, H. R., AND T. DU. 2001. Light scattering by nonspherical particles: Application to coccoliths detached from *Emiliania huxleyi*. Limnol. Oceanogr. **46:** 1438–1454, doi:10.4319/lo.2001.46.6.1438

HATCHER, A., P. HILL, AND J. GRANT. 2001. Optical backscatter of marine flocs. J. Sea Res. **46:** 1–12, doi:10.1016/S1385-1101(01)00066-1

HILL, P. S., E. BOSS, J. P. NEWGARD, B. A. LAW, AND T. G. MILLIGAN. 2011. Observations of the sensitivity of beam attenuation to particle size in a coastal bottom boundary layer. J. Geophys. Res. **116:** C02023, doi:10.1029/2010JC006539

———, C. R. SHERWOOD, R. W. STERNBERG, AND A. R. M. NOWELL. 1994. In-situ measurements of particle settling velocity on the northern California continental shelf. Cont. Shelf Res. **14:** 1123–1137, doi:10.1016/0278-4343(94)90031-0

INTERNATIONAL ORGANIZATION FOR STANDARDIZATION (ISO). 1999. Water quality—determination of turbidity. ISO **7027:** 1999(E).

JONASZ, M. 1983. Particle-size distributions in the Baltic. Tellus B **35:** 346–358, doi:10.1111/j.1600-0889.1983.tb00039.x

JOUON, A., S. OUILLON, P. DOUILLET, J. P. LEFEBVRE, J. M. FERNANDEZ, X. MARI, AND J. M. FROIDEFOND. 2008. Spatiotemporal variability in suspended particulate matter concentration and the role of aggregation on size distribution in a coral reef lagoon. Mar. Geol. **256:** 36–48, doi:10.1016/j.margeo.2008.09.008

KITCHEN, J. C., AND J. R. V. ZANEVELD. 1992. A 3-layered sphere model of the optical-properties of phytoplankton. Limnol. Oceanogr. **37:** 1680–1690, doi:10.4319/lo.1992.37.8.1680

LATIMER, P. 1985. Experimental tests of a theoretical method for predicting light scattering by aggregates. Appl. Opt. **24:** 3231–3239, doi:10.1364/AO.24.003231

LOISEL, H., B. LUBAC, D. DESSAILLY, L. DUFORET-GAURIER, AND V. VANTREPOTTE. 2010. Effect of inherent optical properties variability on the chlorophyll retrieval from ocean color remote sensing: An in situ approach. Opt. Express **18:** 20949–20959, doi:10.1364/OE.18.020949

———, X. MERIAUX, J. F. BERTHON, AND A. POTEAU. 2007. Investigation of the optical backscattering to scattering ratio of marine particles in relation to their biogeochemical composition in the eastern English Channel and southern North Sea. Limnol. Oceanogr. **52:** 739–752, doi:10.4319/lo.2007.52.2.0739

———, ———, A. POTEAU, L. F. ARTIGAS, B. LUBAC, A. GARDEL, J. CAFFLAUD, AND S. LESOURD. 2009. Analyze of the inherent optical properties of French Guiana coastal waters for remote sensing applications. J. Coast. Res. **56:** 1532–1536.

———, AND A. MOREL. 1998. Light scattering and chlorophyll concentration in case 1 waters: A reexamination. Limnol. Oceanogr. **43:** 847–858, doi:10.4319/lo.1998.43.5.0847

MARTINEZ-VICENTE, V., P. E. LAND, G. H. TILSTONE, C. WIDDICOMBE, AND J. R. FISHWICK. 2010. Particulate scattering and backscattering related to water constituents and seasonal changes in the Western English Channel. J. Plankton Res. **32:** 603–619, doi:10.1093/plankt/fbq013

MCKEE, D., M. CHAMI, I. BROWN, V. S. CALZADO, D. DOXARAN, AND A. CUNNINGHAM. 2009. Role of measurement uncertainties in observed variability in the spectral backscattering ratio: A case study in mineral-rich coastal waters. Appl. Opt. **48:** 4663–4675, doi:10.1364/AO.48.004663

———, AND A. CUNNINGHAM. 2006. Identification and characterisation of two optical water types in the Irish Sea from in situ inherent optical properties and seawater constituents. Estuar. Coast. Shelf Sci. **68:** 305–316, doi:10.1016/j.ecss.2006.02.010

MIKKELSEN, O. A., AND M. PEJRUP. 2000. In situ particle size spectra and density of particle aggregates in a dredging plume. Mar. Geol. **170:** 443–459, doi:10.1016/S0025-3227(00)00105-5

MOREL, A. 1973. Diffusion de la lumière par les eaux de mer; résultats expérimentaux et approche théorique. *In* Optics of the sea, interface, and in-water transmission and imaging. AGARD Lecture Series No. 61. [The scattering of light by sea water: Experimental results and theoretical approach]

———, AND Y. H. AHN. 1991. Optics of heterotrophic nano-flagellates and ciliates—a tentative assessment of their scattering role in oceanic waters compared to those of bacterial and algal cells. J. Mar. Res. **49:** 177–202, doi:10.1357/002224091784968639

———, AND A. BRICAUD. 1981. Theoretical results concerning light-absorption in a discrete medium, and application to specific absorption of phytoplankton. Deep-Sea Res. I **28:** 1375–1393.

———, AND ———. 1986. Inherent optical properties of algal cells, including picoplankton. Theoretical and experimental results. Can. Bull. Fish. Aquat. Sci. **214:** 521–559.

NECHAD, B., K. G. RUDDICK, AND Y. PARK. 2010. Calibration and validation of a generic multisensor algorithm for mapping of total suspended matter in turbid waters. Remote Sens. Environ. **114:** 854–866, doi:10.1016/j.rse.2009.11.022

OUBELKHEIR, K. J., H. CLAUSTRE, A. SCIANDRA, AND M. BABIN. 2005. Bio-optical and biogeochemical properties of different trophic regimes in oceanic waters. Limnol. Oceanogr. **50:** 1795–1809, doi:10.4319/lo.2005.50.6.1795

PAK, H., G. F. BEARDSLEY, G. R. HEATH, AND H. CURL. 1970. Light-scattering vectors of some marine particles. Limnol. Oceanogr. **15:** 683–687, doi:10.4319/lo.1970.15.5.0683

————, AND J. R. V. ZANEVELD. 1977. Bottom nepheloid layers and bottom mixed layers observed on continental-shelf off Oregon. J. Geophys. Res. **82:** 3921–3931, doi:10.1029/JC082i027p03921

PEGAU, W. S., D. GRAY, AND J. R. V. ZANEVELD. 1997. Absorption and attenuation of visible and near-infrared light in water: Dependence on temperature and salinity. Appl. Opt. **36:** 6035–6046, doi:10.1364/AO.36.006035

PENG, F., AND S. W. EFFLER. 2007. Suspended minerogenic particles in a reservoir: Light-scattering features from individual particle analysis. Limnol. Oceanogr. **52:** 204–216, doi:10.4319/lo.2007.52.1.0204

————, AND ————. 2010. Characterizations of individual suspended mineral particles in western Lake Erie: Implications for light scattering and water clarity. J. Great Lakes Res. **36:** 686–698, doi:10.1016/j.jglr.2010.08.003

REYNOLDS, R. A., D. STRAMSKI, V. M. WRIGHT, AND S. B. WOŹNIAK. 2010. Measurements and characterization of particle size distributions in coastal waters. J. Geophys. Res. **115:** C08024, doi:10.1029/2009JC005930

ROESLER, C., AND E. BOSS. 2008. In situ measurement of the inherent optical properties (IOPs) and potential for harmful algal bloom detection and coastal ecosystem observations, p. 153–206. *In* M. Babin, C. Roesler, and J. Cullen [eds.], Real-time coastal observing systems for marine ecosystem dynamics and harmful algal blooms: Theory, instrumentation and modelling. UNESCO.

SLADE, W. H., E. BOSS, AND C. RUSSO. 2011. Effects of particle aggregation and disaggregation on their inherent optical properties. Opt. Express **19:** 7945–7959, doi:10.1364/OE.19.007945

SNYDER, W. A., AND OTHERS. 2008. Optical scattering and backscattering by organic and inorganic particulates in US coastal waters. Appl. Opt. **47:** 666–677, doi:10.1364/AO.47.000666

SPINRAD, R. W., J. R. V. ZANEVELD, AND J. C. KITCHEN. 1983. A study of the optical characteristics of the suspended particles in the benthic nepheloid layer of the Scotian Rise. J. Geophys. Res. **88:** 7641–7645, doi:10.1029/JC088iC12p07641

STRAMSKI, D., M. BABIN, AND S. B. WOŹNIAK. 2007. Variations in the optical properties of terrigenous mineral-rich particulate matter suspended in seawater. Limnol. Oceanogr. **52:** 2418–2433, doi:10.4319/lo.2007.52.6.2418

————, E. BOSS, D. BOGUCKI, AND K. J. VOSS. 2004. The role of seawater constituents in light backscattering in the ocean. Prog. Oceanogr. **61:** 27–56, doi:10.1016/j.pocean.2004.07.001

————, AND D. A. KIEFER. 1991. Light-scattering by microorganisms in the open ocean. Prog. Oceanogr. **28:** 343–383, doi:10.1016/0079-6611(91)90032-H

————, AND A. MOREL. 1990. Optical properties of photosynthetic picoplankton in different physiological states as affected by growth irradiance. Deep-Sea Res. I **37:** 245–266.

————, A. SCIANDRA, AND H. CLAUSTRE. 2002. Effects of temperature, nitrogen, and light limitation on the optical properties of the marine diatom *Thalassiosira pseudonana*. Limnol. Oceanogr. **47:** 392–403, doi:10.4319/lo.2002.47.2.0392

SULLIVAN, J. M., AND M. S. TWARDOWSKI. 2009. Angular shape of the oceanic particulate volume scattering function in the backward direction. Appl. Opt. **48:** 6811–6819, doi:10.1364/AO.48.006811

————, ————, P. L. DONAGHAY, AND S. A. FREEMAN. 2005. Use of optical scattering to discriminate particle types in coastal waters. Appl. Opt. **44:** 1667–1680, doi:10.1364/AO.44.001667

————, ————, J. R. V. ZANEVELD, C. M. MOORE, A. H. BARNARD, P. L. DONAGHAY, AND B. RHOADES. 2006. Hyperspectral temperature and salt dependencies of absorption by water and heavy water in the 400–750-nm spectral range. Appl. Opt. **45:** 5294–5309, doi:10.1364/AO.45.005294

TRAYKOVSKI, P., R. J. LATTER, AND J. D. IRISH. 1999. A laboratory evaluation of the laser in situ scattering and transmissometery instrument using natural sediments. Mar. Geol. **159:** 355–367, doi:10.1016/S0025-3227(98)00196-0

TWARDOWSKI, M. S., E. BOSS, J. B. MACDONALD, W. S. PEGAU, A. H. BARNARD, AND J. R. V. ZANEVELD. 2001. A model for estimating bulk refractive index from the optical backscattering ratio and the implications for understanding particle composition in case I and case II waters. J. Geophys. Res. **106:** 14129–14142, doi:10.1029/2000JC000404

ULLOA, O., S. SATHYENDRANATH, AND T. PLATT. 1994. Effect of the particle-size distribution on the backscattering ratio in seawater. Appl. Opt. **33:** 7070–7077, doi:10.1364/AO.33.007070

VAILLANCOURT, R. D., C. W. BROWN, R. R. L. GUILLARD, AND W. M. BALCH. 2004. Light backscattering properties of marine phytoplankton: Relationships to cell size, chemical composition and taxonomy. J. Plankton Res. **26:** 191–212, doi:10.1093/plankt/fbh012

VAN DE HULST, H. C. 1957. Light scattering by small particles. John Wiley.

VAN DER LINDE, D. W. 1998. Protocol for determination of total suspended matter in oceans and coastal zones. JRC Technical Note I.98.182.

VANTREPOTTE, V., AND OTHERS. *In press.* Seasonal and interannual (2002–2010) variability of the suspended particulate matter as retrieved from satellite ocean color sensor over the French Guiana coastal waters. J. Coastal Res.

VOLTEN, H., AND OTHERS. 1998. Laboratory measurements of angular distributions of light scattered by phytoplankton and silt. Limnol. Oceanogr. **43:** 1180–1197, doi:10.4319/lo.1998.43.6.1180

WELLS, J. T., AND S. Y. KIM. 1991. The relationship between beam transmission and concentration of suspended particulate material in the Neuse river estuary, North Carolina. Estuaries **14:** 395–403, doi:10.2307/1352264

WELLS, M. L., AND E. D. GOLDBERG. 1994. The distribution of colloids in the North Atlantic and Southern Oceans. Limnol. Oceanogr. **39:** 286–302, doi:10.4319/lo.1994.39.2.0286

WOŹNIAK, S. B., AND D. STRAMSKI. 2004. Modeling the optical properties of mineral particles suspended in seawater and their influence on ocean reflectance and chlorophyll estimation from remote sensing algorithms. Appl. Opt. **43:** 3489–3503, doi:10.1364/AO.43.003489

————, AND OTHERS. 2010. Optical variability of seawater in relation to particle concentration, composition, and size distribution in the nearshore marine environment at Imperial Beach, California. J. Geophys. Res. **115:** C08027, doi:10.1029/2009JC005554

YORK, D. 1966. Least-squares fitting of a straight line. Can. J. Phys. **44:** 1079–1086, doi:10.1139/p66-090

ZHANG, X. D., L. B. HU, M. S. TWARDOWSKI, AND J. M. SULLIVAN. 2009. Scattering by solutions of major sea salts. Opt. Express **17:** 19580–19585, doi:10.1364/OE.17.019580